A supervised data-driven spatial filter denoising method for acoustic-induced artifacts in intracranial electrophysiological recordings

Victoria Peterson[1,2*], Matteo Vissani[1*], Shiyu Luo[3], Qinwan Rabbani[4], Nathan E. Crone[5], Alan Bush[1], R. Mark Richardson[1,6]

[1]Department of Neurosurgery, Massachusetts General Hospital, Harvard Medical School, Boston, United States
[2]Instituto de Matemática Aplicada del Litoral, IMAL, FIQ-UNL, CONICET, Santa Fe, Argentina
[3]Department of Biomedical Engineering, The Johns Hopkins University School of Medicine
[4]Department of Electrical & Computer Engineering, The Johns Hopkins University
[5]Department of Neurology, The Johns Hopkins University School of Medicine
[6]Department of Brain and Cognitive Sciences, Massachusetts Institute of Technology, Cambridge, Massachusetts, United States

Abstract

Neurosurgical procedures, in which electrodes can be placed in the brain of awake patients, offer remarkable opportunities to discover the neurophysiology underlying human speech. The relative scarcity of these opportunities and the altruism of participating patients obligates us to apply the highest possible rigor to signal interpretation. Intracranial electroencephalography (iEEG) signals recorded during overt speech can present an acoustic-induced vibration artifact that tracks the fundamental frequency (F0) of the participant's voice, encompassing high-gamma frequencies that are used for neural activation during speech production and perception. To advance our understanding of the neural control of speech production and develop reliable speech models, we developed a spatial filtering approach to identify and remove acoustic-induced artifactual components of the recorded signal. We show that traditional reference schemes may jeopardize signal quality, but our data-driven method can denoise the recording while preserving signals from the underlying neural activity.

Key words

Speech production, Vibration Artifact, iEEG, Spatial Filtering, Phase-Coupling Optimization

List of abbreviations

Abbreviation	Definition
AGR	Artifact to physiological gamma ratio
BCI	Brain-computer interfaces
CAR	Common average reference
CAS	Colored noise audio scenario
CS	Cosine similarity
DBS	Deep brain stimulation

[*] Equal contribution

ECoG	Electrocorticography
EEG	Electroencephalography
F0	Fundamental frequency of the voice
FWHM	Full width at half maximum
ICA	Independent component analysis
iEEG	Intracranial electroencephalography
LFP	Local field potentials
LIF	Leaky integrate and fire
MCAS	Modulated colored noise audio scenario
MSCE	Magnitude squared coherence estimate
MVL	Mean vector length
PC	Principal component
PCA	Principal component analysis
PCD	Phase-coupling decomposition
PCO	Phase-coupling optimization
PLP	Perceptual linear prediction
PR	Participation ratio
RAS	Recorded audio scenario
SAS	Sinusoidal audio scenario
SNR	Signal-to-noise ratio
SSD	Spatio-spectral decomposition
VAFB	Vibration artifact frequency band

Main

Human intracranial recordings, i.e. in-vivo electrophysiological signals acquired during specific neurosurgical treatments such as focal epilepsy and deep brain stimulation (DBS), have enabled the study of neural responses with high temporal and spatial resolution, in both surface and deep structures of the human brain during behavioral tasks[1]. The study of speech production especially benefits from awake intraoperative recordings during which local field potentials (LFP) and single unit activity of subcortical targets can be simultaneously acquired during speech production[2,3].

To develop brain-computer interfaces (BCI) for speech protheses, the neural activity in the high gamma band (60-200 Hz) is typically used for speech decoders[4–7]. Recently, we and others have shown that brain activity measured even with invasive recordings may contain artifacts associated with the mechanical vibrations produced by the participant's voice or sounds played by a loudspeaker[8,9]. For overt speech experiments, this vibration artifact shares spectral characteristics with the produced audio signal, being locked at the fundamental frequency (F0) of the participant's voice[8]. The overlap between typical human

F0 values (between 70 and 240 Hz) and high-gamma activity (60 to 250Hz) imposes the need to account for the vibration artifact to study the brain activity associated with speech production.

In the case of speech tasks performed during stereotactic neurosurgery, the patient's head is fixed to a stereotactic frame (Fig. 1a). This frame may act as a resonance system of unknown transfer function that exacerbates speech-induced vibrations originating in the larynx and travelling through the head and skull. Speech-induced vibrations, which look like a distorted version of the speech audio, can affect the electrodes and/or acquisition chain and appear in the neural recordings, tracking the fundamental frequency of the participant's voice (Fig. 1b). Considering the recorded brain activity as superpositions of different uncorrelated statistical sources[10], the brain signals at the amplifier level can be thought of as the consequence of a linear mix between true neurophysiological and non-neural sources, including speech-induced vibrations (Fig. 1c). Using spatial filter methods, these sources can be untangled and estimated from the multivariate (multichannel) electrode signals[11]. As such, traditional re-referencing schemes used in neurophysiology, like bipolar, Laplacian, or common average reference (CAR), can be reframed as spatial filtering approaches, in which the recorded brain signals are multiplied by a predefined matrix that references the recording of one electrode with respect to a neighborhood of channels[12] (see CAR as a spatial filtering algorithm, Methods).

Acoustic-induced vibration artifacts can be detected by measuring the coherence value between the speech acoustic signal and neural recordings in the high-gamma frequency band[8]. The coherence value between the audio signal and a neural channel recording largely varies between and within patients, indicating that the vibration artifact is a channel-specific type of noise, and thus traditional re-reference schemes may jeopardize the quality of the neural recordings[13].

Data-driven spatial filters offer a more flexible re-reference scheme than traditional methods. They can be used for denoising, using linear transformations to

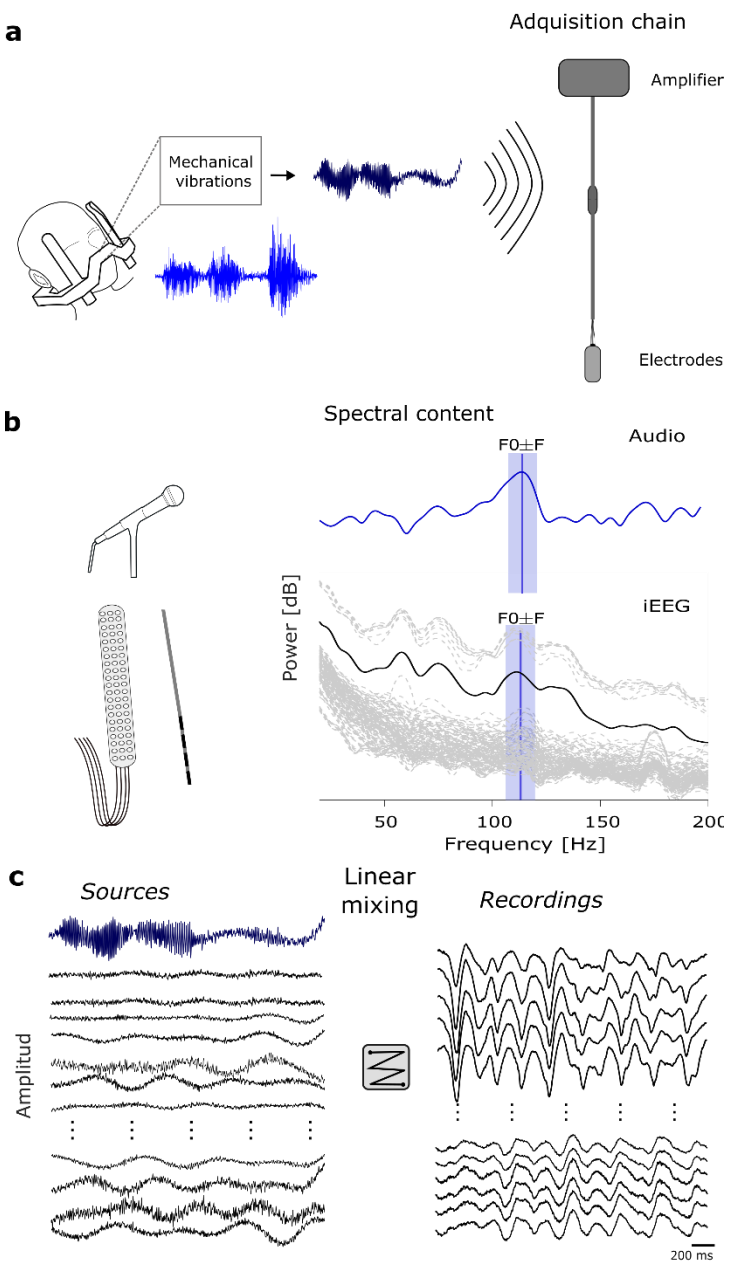

Fig. 1| Speech-induced vibration artifact model assumptions. **a,** Schematic representation of how speech-induced mechanical vibrations can affect neural recordings. The frame attached to the patient's head acts as a resonance system with the skull, transmitting and distorting speech-induced vibrations that can affect the neural recordings' acquisition chain. **b**, The vibration artifact tracks the fundamental frequency (F0) of the participant's voice. **c**, The recordings, at the amplifier level, can be thought as a linear mixing between the vibration artifact and brain-related sources.

estimate the data subspace related to "noise" and discard it for the subsequent signal analyses[12,14,15]. This approach has been used primarily for non-invasive electrophysiology[12,14,16,17], and more recently for iEEG signal processing[11,18,19]. A typical pipeline for artifact removal in non-invasive EEG consists of using principal component analysis (PCA) and independent component analysis (ICA) for identifying artifact components[16,20]. PCA is commonly used as a dimensionality reduction tool to alleviate the decomposition done by ICA. Then, by means of low-rank factorization, backward and forward projections are made between the signal and the source space, identifying and discarding those components related to artifacts. However, due to the nature of the speech-induced vibration artifact, which overlaps in frequency with high-gamma activity, ICA may fail to decompose artifactual from neural sources[21] (see also Results Section).

Here, we introduce phase-coupling decomposition (PCD), an algorithm for acoustic-induced artifact rejection. This algorithm performs data-driven spatial filtering denoising based on low-rank factorization. It is designed to separate acoustic-induced artifactual sources from neural sources via a phase-coupling decomposition. The spatio-spectral decomposition (SSD)[21] algorithm is used first to enhance signal-to-noise ratio around F0 and perform dimensionality reduction. The phase-coupling optimization (PCO)[22] method is then applied to identify sources phase-locked to the acoustic signal. Thus, the coherence between the audio and the neural data is optimized, allowing retrieval of those sources related to acoustic-induced noise. Similar to the ICA-based artifact pipeline mentioned above, signal reconstruction is based on low-rank factorization, discarding the detected artifactual components.

First, we demonstrate how PCD cleans acoustic-induced artifacts from an affected recording (Fig. 2). Then, we test the denoising performance of this algorithm in simulated data, in which the artifact and the neural sources are artificially generated and mixed. The algorithm successfully recovers the artifactual source, in the time, frequency, and phase domains even when dealing with highly non-stationary audio signals (Fig. 3). In addition, we demonstrate the algorithm's ability to denoise while preserving neural data and compare its performance with respect to traditional spatial filtering methods like CAR and ICA (Fig. 4). Finally, we test the PCD denoising algorithm in real acoustic contaminated iEEG data, showing an important reduction of the extent and number of artifact-affected electrodes (Fig. 5).

Box 1 | Phase Coupling Decomposition

Given the recorded brain activity $\boldsymbol{X} \in \mathbb{R}^{N_c \times N_s}$, where N_c and N_s are the number of channels and samples, respectively, and the acoustic signal $\boldsymbol{z} \in \mathbb{R}^{N_s}$, this algorithm identifies narrow-band components of $\boldsymbol{X}$ that are phase-coupled with $\boldsymbol{z}$.

Step 1: Estimate the vibration artifact bandwidth.

1. Calculate the power spectrum of $\boldsymbol{z}$.
2. Around the fundamental frequency (F0) of the participant's voice, find the peak in the spectra (P_{F0}).
3. Define the center P_{F0} and bandwidth of the vibration artifact frequency band (VAFB): $F_c \pm \Delta F_c$.

Step 2: Find projections of $\boldsymbol{X}$ that maximize the signal-to-noise-ratio (SNR) around F_c via the spatio-spectral decomposition[21] (SSD).

1. Define as *signal band* the VAFB: $F_c \pm \Delta F_c$, and as *noise band all frequencies* except VAFB. Find the projection matrix $\boldsymbol{W}_{SSD}$ by solving equation (3) and project the data on the first k SSD components $\widetilde{\boldsymbol{W}}_{SSD} = [\boldsymbol{w_1}, \dots, \boldsymbol{w_k}]$, as follows: $\widetilde{\boldsymbol{X}}_{SSD} = \widetilde{\boldsymbol{W}}_{SSD}^{\boldsymbol{T}} \boldsymbol{X}$.

Step 3: Find the artifactual sources via the phase-coupling optimization algorithm[22] (PCO).

1. In the SSD space, find the projection matrix $\boldsymbol{W}_{PCO}$ which maximizes the mean vector length (see equation (6) and (7)) between $\widetilde{\boldsymbol{X}}_{SSD}$ and $\boldsymbol{z}$.
2. Compute the PCO components $\boldsymbol{X}_{PCO} = \boldsymbol{W}_{PCO}^{\boldsymbol{T}} \boldsymbol{X}_{SSD}$ and identify the m acoustic-induced sources.

Step 4: Perform the denoising via low-rank factorization.

1. Compute the PCD unmixing matrix $\boldsymbol{W}_{PCD}$ which projects $\boldsymbol{X}$ to the artifact source space. This matrix is the conjunction of both $\boldsymbol{W}_{PCO}$ and $\boldsymbol{W}_{SSD}$ (equation (8)).
2. Compute the PCD mixing matrix via the pseudoinverse:
$$\boldsymbol{A}_{PCD} = \boldsymbol{W}_{PCD}^{\dagger}$$
3. Reconstruct the signal by using $(N_c - m)$ components: $\boldsymbol{X}_{denoised} = \widetilde{\boldsymbol{A}}_{PCD} \widetilde{\boldsymbol{W}}_{PCD}^{\boldsymbol{T}} \boldsymbol{X}$.

See details in the Methods and Extended Data Fig. 1 for a visualization of the pipeline.

Results

Overview of phase-coupling decomposition. Here, we provide a summary of the PCD pipeline (Box 1, Extended Data Fig. 1, Methods). We consider the brain recordings as a linear combination of statistical sources, where at least one of those sources is related to the vibration artifact, which can be detected by measuring the coherence value between the audio signal and the neural recordings[8]. The recorded brain signals then are considered as terms of a linear forward model, in which N_C statistical sources are projected into N_C channels along the N_S data samples via a linear mixing process:

$$\mathbf{X} = \mathbf{AS}, \qquad (1)$$

where $\boldsymbol{X} \in \mathbb{R}^{N_c \times N_s}$ denotes the recorded brain signals, $\boldsymbol{S} \in \mathbb{R}^{N_c \times N_s}$ is the source activity, and $\boldsymbol{A} \in \mathbb{R}^{N_c \times N_c}$ denotes the mixing matrix. Each column $\boldsymbol{a}$ of the mixing matrix $\boldsymbol{A}$ is known as *spatial pattern* and describes the projection of an individual source to the sensor space.

The idea of PCD is to find the artifactual sources that are phase-coupled with the acoustic signal, denoted here as $\mathbf{z} \in \mathbb{R}^{N_s}$. The first step within the PCD pipeline is to estimate the vibration artifact frequency band (VAFB). To this end, since the vibration artifact tracks F0, the power spectrum of the acoustic signal can be used (Step 1 Box 1, Extended Data Fig. 1a). Once VAFB is estimated, the spatio-spectral decomposition (SSD) algorithm (Methods)[21] is applied to (i) enhance the power around the VAFB and (ii) reduce the dimensionality of the data (Step 2 Box 1, Extended Data Fig. 1b).

Data projected onto the first k SSD components, showing the largest power at the VAFB, are used for the phase-coupling optimization (PCO)

algorithm[22] (Methods), in which an index of coherence between the data on the SSD space $\boldsymbol{X}_{SSD}$ and the acoustic signal $\boldsymbol{z}$ is maximized (Step 3 Box 1, Extended Data Fig. 1c). Following previous work[20], we refer to this index of coherence as the Mean Vector Length (MVL, see Methods equation (6)). Those components showing the highest coherence with the acoustic signal are considered as vibration artifact sources and will be excluded during signal reconstruction (Step 4 Box 1, Extended Data Fig. 1d-e).

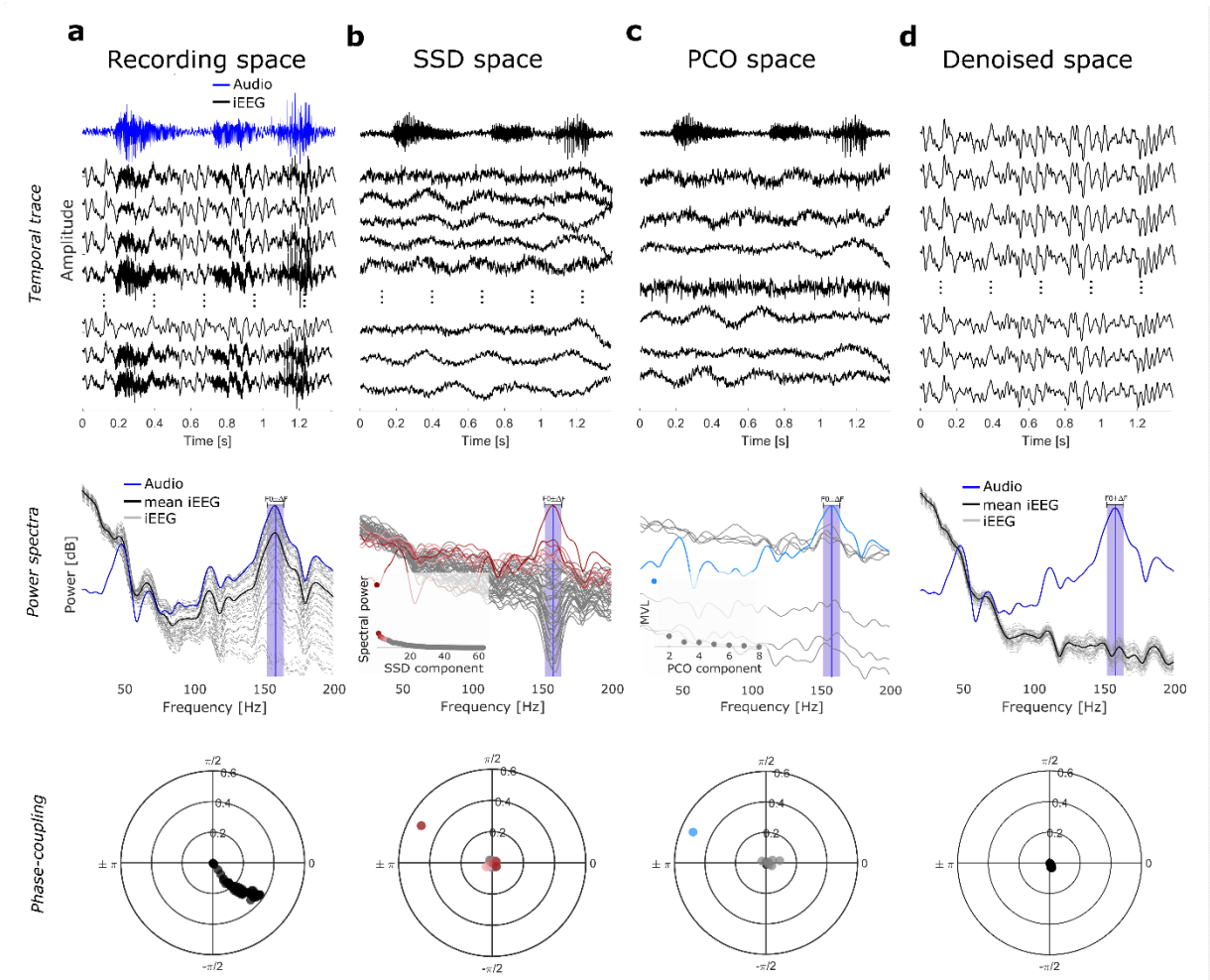

Fig. 2. | Illustration of the phase-coupling decomposition pipeline. Space transformations from the recording space to the clean space in the temporal, power, and phase domains. a, (Recording space), Intracranial brain recordings (iEEG) were combined with the recorded audio to simulate the contaminated recordings for illustration purposes. The audio signal is shown in blue. Around the fundamental frequency (F0) of the participant's voice, a matching peak is observed between the audio and the iEEG power spectra. In the polar plot, a phase-coupling value between the audio signal and the brain recordings that is different from zero is observed for most of the channels (represented as dots). **b,** (SSD space), SSD identifies components that maximize power around F0 (color-coded in the spectral domain from dark red to light pink). **c,** (PCO space), The SSD components with the strongest power around F0 are used to compute PCO. The mean vector length (MVL, an index of coherence with acoustic signals) is optimized and only those PCO components that show the highest MVL are identified as artifactual. Here, the first 8 components are shown **d,** (Denoised space), Via low rank-factorization, the artifactual component(s) are excluded for signal reconstruction. The iEEG in the denoised space depicts a clean temporal trace, with no peak around F0 in the power spectra as well as phase-coupling values centered at zero.

Fig. 2 depicts how contaminated recordings are denoised by applying PCD, in the temporal, spectral and phase domains. For illustration purposes, we artificially contaminated iEEG recordings with an audio signal (Recording space, Fig. 2a), resulting in iEEG signals with a strong peak in spectral power

around F0 (Fig 2a center), together with a consistent phase-relationship with the acoustic signal (Fig 2a bottom). After SSD is applied, only a few components have enhanced power spectra around F0 (Fig. 2b center). Applying PCO in the SSD space gives us components maximally phase-coupled with the recorded audio (Fig. 2c bottom). The components identified as artifactual will be discarded for signal reconstruction, thus achieving a denoised signal (Fig. 2d).

Method benchmarking on in-silico data

To benchmark our method's denoising performance we applied PCD on simulated neural data with added simulated vibration artifact. This approach allows direct comparison of denoised data to the ground-truth simulated neural signals. Briefly, we simulated recurrent networks of leaky integrate-and-fire (LIF) neurons (N = 5000, 80% excitatory and 20% inhibitory) to simulate 100 physiological broadband γ-source activities, defined as the summation of absolute values of the excitatory and inhibitory currents entering the excitatory neurons population (Extended Data Fig. 2, Methods). The model captures key features of physiological LFPs, including (i) the entrainment of the low-frequency fluctuations to the external input, (ii) the internal resonance of broadband γ-oscillations driven by the mean rate of the external input (Extended Data Fig. 3) and (ii) phase-amplitude coupling between low and high frequency oscillations (Supplementary Fig. 1). We defined a single simulated vibration artifact source assuming that it is identical to the produced audio signal, denoted as $\mathbf{z}$ in the PCD pipeline. After adjusting the artifact-to-physiological gamma ratio (AGR), we linearly projected the sources to the simulated recordings by the application of a random mixing matrix. We tested the PCD pipeline in different simulation scenarios based on the expression of the external input driving LIF neurons and the audio source (Extended Data Fig. 2, Methods).

Toy examples

Simulations were composed of a stationary external neural input (i.e., superposition of a sustained and periodically modulated inputs) and different expressions for the vibration artifact source: pure sinusoidal (SAS), colored noise (CAS) and modulated colored noise (MCAS). We assessed the robustness of the PCD pipeline by sweeping key parameters of the model within a meaningful range (see details in Methods). The algorithm's performance was quantified by different metrics that describe (i) the agreement in the temporal domain between the denoised neural signals and the ground-truth neural signals ($log(\chi)$) (see Methods equation (9)), (ii) the magnitude coherence estimate (MSCE, see Methods equation (10))**,** and (iii) the phase-locking value (PLV) between the estimated vibration artifact source and $\boldsymbol{z}$ (see Methods equation (11)). For pure sinusoidal artifacts, PCD perfectly removed the artifact regardless of the AGR, fundamental frequency and number of channels (Supplementary Figs. 2-3). For the colored noise artifact, simulations suggested a small decrease of performance with broadband artifacts, which is consistent with known limitations of SSD (Supplementary Fig. 4, Extended Data Fig 4). Finally, PCD yielded robust performances when tested with modulated colored noise artifact simulations (Supplementary Fig. 5).

Realistic scenario

To test the method under more realistic conditions, we modulated the external input to the neural source to mimic observed γ-band activity during 60 trials of a speech production task (Supplementary Fig. 6). Neural sources were mixed (at a range of AGRs) with recorded audio of Parkinson's Disease patients during an intraoperative speech task (Supplementary Fig. 7). PCD reliably recovered the artifactual source, as can be observed in the time, frequency, and time-frequency profiles of both the true (Fig. 3a) and estimated (Fig. 3b) artifact source. Across trials, no differences were found at any sample point between the true and the estimated artifact source, as assessed by one-dimensional statistical parametric mapping (SPM1d, https://spm1d.org/), (Fig. 3c). The estimated artifactual source had high coherence with the true artifactual source at frequencies around F0 (mean MSCE > 0.97, Fig. 3d),

independently of differences in the AGR (Supplementary Fig. 8). Finally, the estimated source was either in phase or anti-phase relationship with respect to the true source (Fig. 3e). Similar results were found for the other realistic simulations (Supplementary Fig. 8).

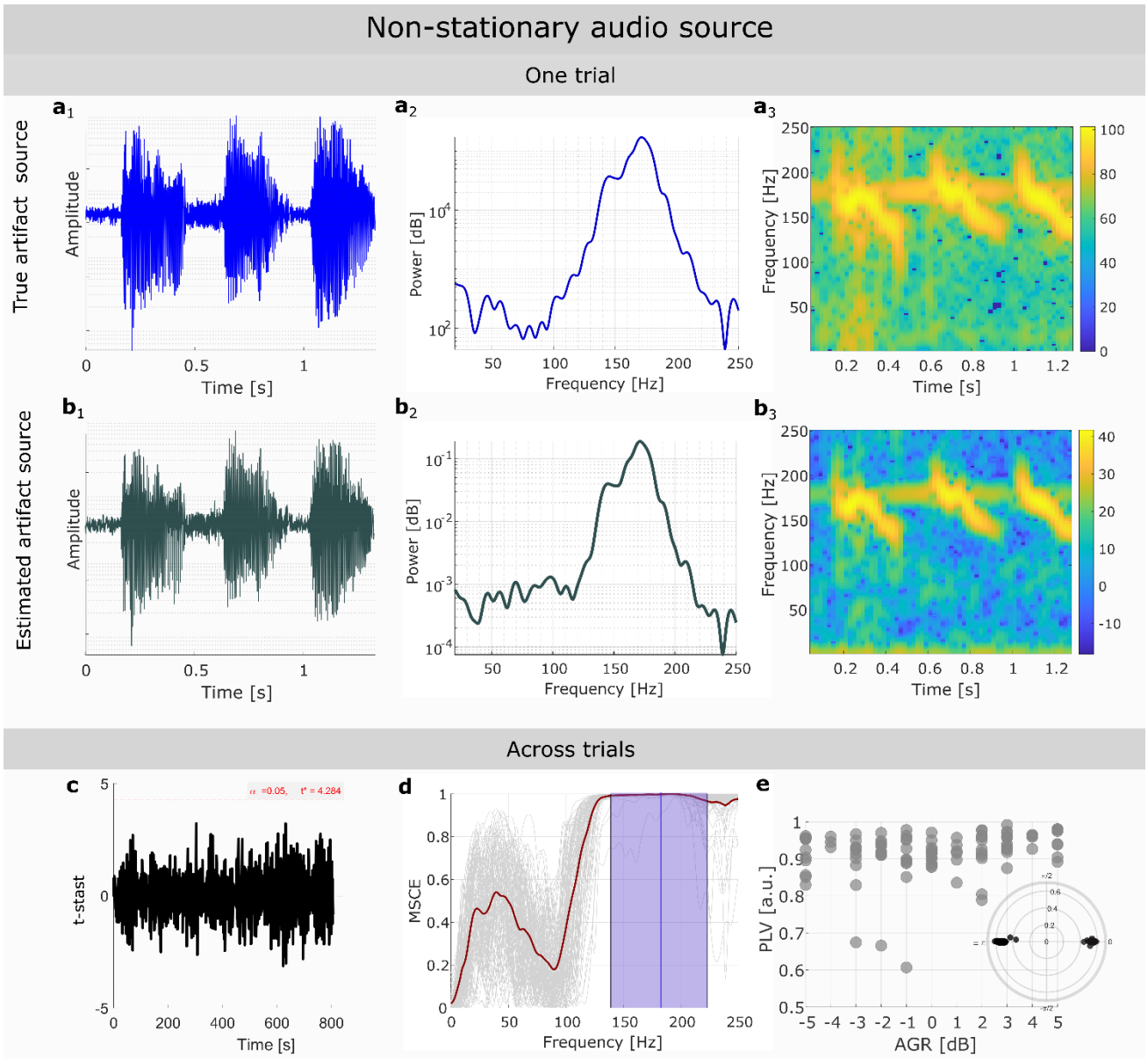

Fig. 3| PCD correctly retrieves non-stationary and weak artifactual sources. Representative performance of PCD on an artifactual source with a non-stationary signal profile and an artifact-to-physiological gamma ratio (AGR) = 2dB. **(Top panel) a1-a3,** Visualization in the time, frequency, and time-frequency domain of the ground-truth artifactual source for a given trial. **b1-b3,** Same as above for the retrieved artifactual source for the same trial. **(Bottom panel),** PCD performance across trials. **c**, One-dimensional statistical parametric mapping was used to evaluate statistical similarities at each sample point between the true and estimated source for each trial. No significant differences (t-stats values < t*) were found at any time point. **d**, Magnitude-squared coherence estimate (MSCE) between true and estimated artifact sources. Gray lines represent individual trials. Mean MSCE across trials is denoted by the dark red line. The mean F0 across trials is shown as the blue vertical line, while the violet band indicates the VAFB. The mean MSCE value in the VAFB was always above 0.97, regardless of the variable AGR across trials. **e**, Phase-locking value (PLV) across simulated trials at different AGR between the true and estimated artifact source, for each trial. Inset on the right corner aggregates the phase difference found across trials between the true and estimated artifact source.

PCD removes the vibration artifact while preserving simulated γ-activity. Next, we compared the performance of PCD with CAR and ICA, two well-known preprocessing spatial filtering approaches, using simulated data under the realistic scenario (see Methods). For a fair comparison, all three methods were implemented on a trial-wise basis and components identified by ICA were scored according to their phase-coupling value against the recorded audio (Methods). We evaluated performance in terms of the capacity of each method to retrieve the temporal, frequency, and phase information of the simulated ground-truth neural data (Fig. 4a-4c). Figure 4 shows the simulated neural activity without the artifact source (Artifact free), when linearly combined with the artifactual source (Contaminated), and the resulting denoised signals from each method (CAR, ICA, PCD). PCD outperformed the other methods in terms of its ability to clean the data and retrieve the simulated brain signals, as can be observed in the time (Fig. 4a), frequency (Fig. 4b) and phase (Fig. 4c) domains. In this simulation CAR produced traces very similar to the contaminated signal, while ICA attenuated the artifact to some extent. Interestingly, PCD completely removed the narrow-band component induced by the vibration artifact while preserving gamma modulation observed in the simulated brain signals.

To assess the preservation of physiological brain signals after denoising, we compared the neural embedding defined in the subspace spanned by the first three PCA components (PC subspace). The PC subspace of the simulated brain signals represents the embedding related to the simulated gamma modulation associated to the speech task. CAR resulted in an embedding indistinguishable from the contaminated signals (Fig. 4d), consistent with the abovementioned time, frequency, and phase analyses. Interestingly, while ICA was able to attenuate the vibration artifact, the PC embedding was different from that for the simulated brain signals, indicating that ICA distorted the underlying physiological sources. Here, PCD was the only algorithm that completely removed the artifactual source, as assessed by the signals' power spectrum (Fig. 4b) and phase coupling (Fig. 4c) plots, while simultaneously preserving the underlying physiological activity, as evidenced by the indistinguishable PC embedding to that of the simulated brain signals (Fig. 4d). To quantitively assess the similarities to the ground-truth PC embedding we used the cosine similarity metric of the three first components (see Methods equation (12)), resulting in values of 0.79, 0.74 and 0.99 for CAR, ICA and PCD, respectively.

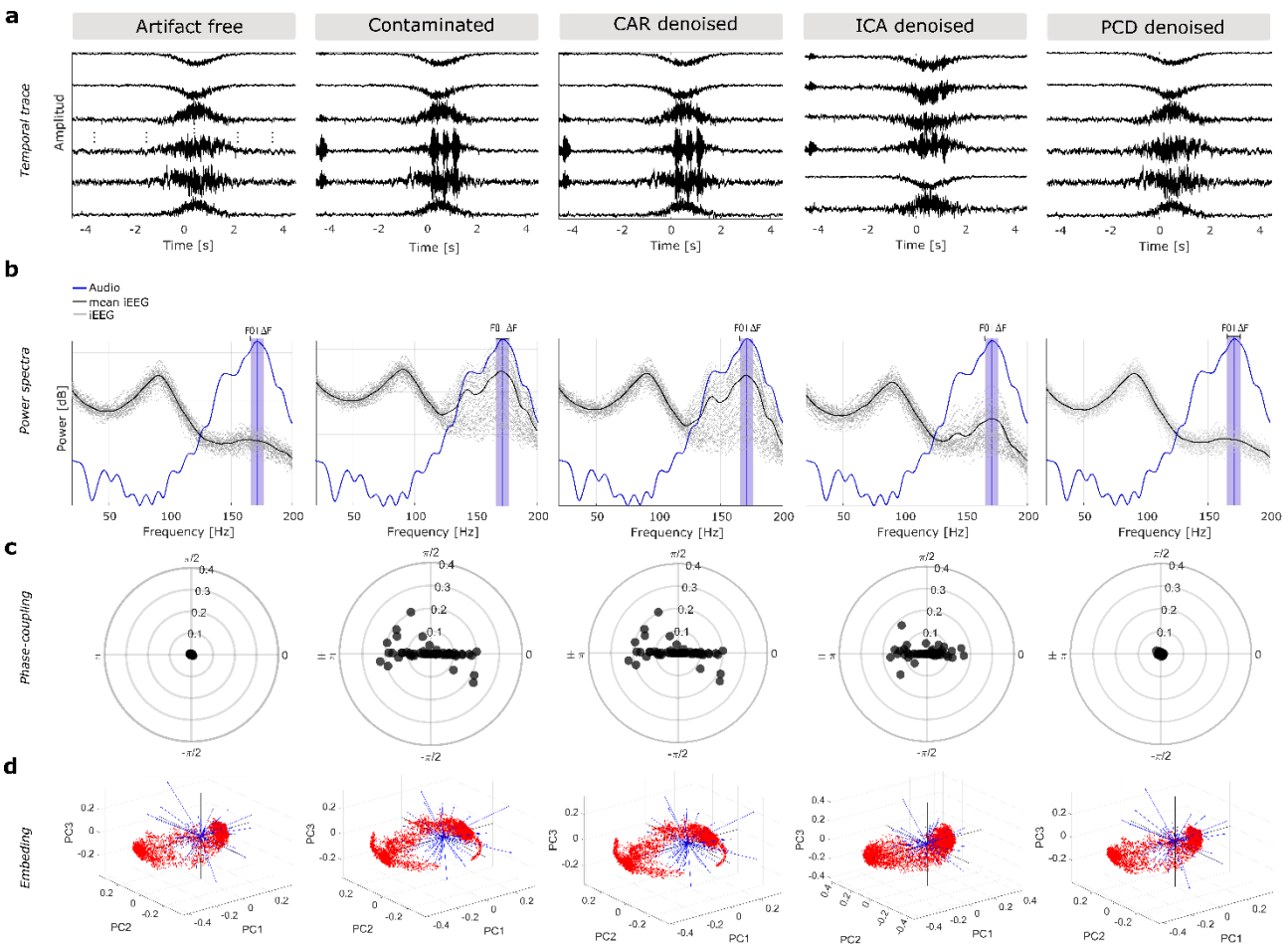

Fig. 4 | PCD removes acoustic-induced vibration artifact while preserving neural activity in simulated data, outperforming previous methods.

For one trial (AGR=-2 dB) of the realistic simulation scenario with low-amplitude broadband gamma modulation and non-stationary artifact source, the impact on signal quality of applying CAR, ICA and PCD is shown. Temporal trace (a), power spectra (b) and phase-coupling plots (c) as in Figure 2. **a**, Resulting temporal traces with time reference relative to the speech onset (t=0). **b**, Power spectrum of each resulting iEEG signal (gray lines) and the recorded audio (blue line). The mean power spectra across iEEG channels is shown by the thick black line. Violet shades indicate the VAFB. **c**, The phase relationship between the audio and the resulting brain signals. Each dot represents a channel. **d**, biplots of the PC subspace described by the first three principal components (PC1, PC2, PC3). Red dots represent scores while blue lines are the loading directions. The shape of the red cloud illustrates the PCA embedding.

Denoising PCD performance in acoustic contaminated iEEG data.
We applied the PCD pipeline to intracranial recordings of 54 patients undergoing DBS implantation surgery who participated in an intraoperative speech task (Methods). Participants were instructed to repeat consonant-vowel syllables triplets played on earphones. Each participant performed between 1 to 4 recording sessions of up to 120 syllable triplets each. High-density electrocorticography (ECoG) from left ventral sensorimotor cortex, superior temporal gyrus and inferior frontal regions were acquired simultaneously with subcortical recordings. Microelectrode recordings (MER) and LFPs from macro rings located 3mm above each microelectrode tip were registered from the subthalamic nucleus (STN) or globus pallidus internus (GPi). LFPs were also registered from DBS lead located either in the STN, GPi or the ventral intermediate nucleus of the thalamus (VIM). As we previously described, around 40% of channels in this dataset show speech-induced vibration artifact [8].

Considering that the source of the vibration artifact is the same across different types of electrodes, the denoising pipeline was applied to all available iEEG recordings together (LFP from ECoG, the DBS lead, and the ring and tip contact of the microelectrode). Given that phase relationships between the recorded audio and the neural recordings are not consistent across trials (Supplementary Fig. 9), data cleaning occurred in a trial-wise manner. The resulting denoised signals were compared to those obtained after applying CAR and ICA (Methods). The number of components to be removed was automatically selected based on the elbow-detection on the MVL values. For a fair comparison, artifactual ICA components were assessed based on the coherence between the components and the recorded audio (Methods). The distribution of Inter-Trial Phase-Consistency (ITPC, see Methods equation (13)) before vs. after applying a denoising framework (Raw vs. CAR, ICA, PCD) was used to assess denoising performance (Fig. 5a). The percentage of clean electrodes (i.e. below the significance threshold of ITPC, horizontal line in Fig. 5a) was used to assess data cleaning (Fig. 5b). Two electrodes from the same participant and trial, reflecting two different scenarios, were selected to illustrate the methods' performances (Fig. 5c). Electrode $ecog_1 49$ is a typical artifactual electrode with a strong narrow band component after speech onset (Fig. 5c top panel), while $ecog_1 59$ is an electrode with a characteristic physiological gamma modulation around the time of speech onset (Fig. 5c bottom panel).

Results show that CAR can jeopardize the signal quality, by shifting the coherence distribution towards higher values (Fig. 5a – CAR). Data degradation can also be observed in the resulting spectrograms, in which the vibration artifact is either artificially introduced or exacerbated after applying CAR due to the presence of the artifact on other electrodes of the ECoG strip (Fig. 5c – CAR). Interestingly, although ICA resulted in a 21.4% median increase in the number of clean electrodes (Fig. 5b – ICA), the low coherence values seem to be related to aggressive high frequency band removal in the data (Fig. 5c – ICA). Although on average 4 components were removed by ICA and PCD, the artifactual sources retrieved by ICA resemble brain activity rather than an acoustic-induced artifact (Extended Data Fig. 5). In the case of PCD, the method achieved a 14.3% median increase in the number of clean electrodes (Fig. 5a – PCD) while preserving physiological gamma modulation when no artifact is present (Fig. 5c – PCD).

To explore if the variability in denoising performance can be explained by characteristics of the artifact across electrodes, we evaluated in Fig. 5d the relationship between the relative gain of clean electrodes by each denoising method, artifact strength and artifact homogeneity (an ITPC-based measure of how similar the artifact is across electrodes, see Methods equations (14) and (15)). Note that recordings

with negative gain (i.e. increased percentage of contaminated electrodes after applying a method) are shown in red (Fig. 5d). CAR has good denoising performance only for highly homogeneous artifacts with a mild to moderate artifact strength (Pearson correlation $r_{gain-homogeneity} = 0.59$, p < 0.0001; $r_{gain-\ strength} = 0.23$, p = 0.006) and can outperform the other methods under these conditions (e.g. Subject A, blue line circles in Fig 5d). Note that CAR can introduce artifact to clean data (e.g. subject C, black line circles in Fig 5d). For ICA, stronger artifacts with mild to moderate homogeneity resulted in higher gain of clean electrodes, as assessed by ITPC ($r_{gain-strength} = 0.57$, p < 0.0001; $r_{gain-homogeneity} = 0.24$, p = 0.003). Interestingly, PCD gain also increases with higher artifact strength but is not significantly correlated with artifact homogeneity ($r_{gain-strength} = 0.50$, p < 0.0001; $r_{gain-homogeneity} = -0.12$, p = 0.14), as illustrated by Subject B (gray line circles in Fig 5d).

Next, we assessed the effect of applying each denoising method as a pre-processing step on decoding performance of a densely-connected convolutional neural network (DenseNet)[23] for consonant decoding (Methods). We tested the decoding method in three different cases: i) CAR and ICA gain is greater than PCD gain (Subject A), ii) PCD outperforms CAR and ICA (Subject B), and iii) data has no artifact (Subject C). Fig. 5e shows that consonant classification accuracy is similar or better when PCD is applied as compared to classification on raw data. Conversely, ICA always decreases classification accuracy, despite increasing the number of clean electrodes as assessed by the ITPC criterion. Interestingly, despite a decrease of the number of clean electrodes after CAR application, consonant classification accuracy improved, suggesting that decoding capacity might be partially driven by the artifact (in Subject B).

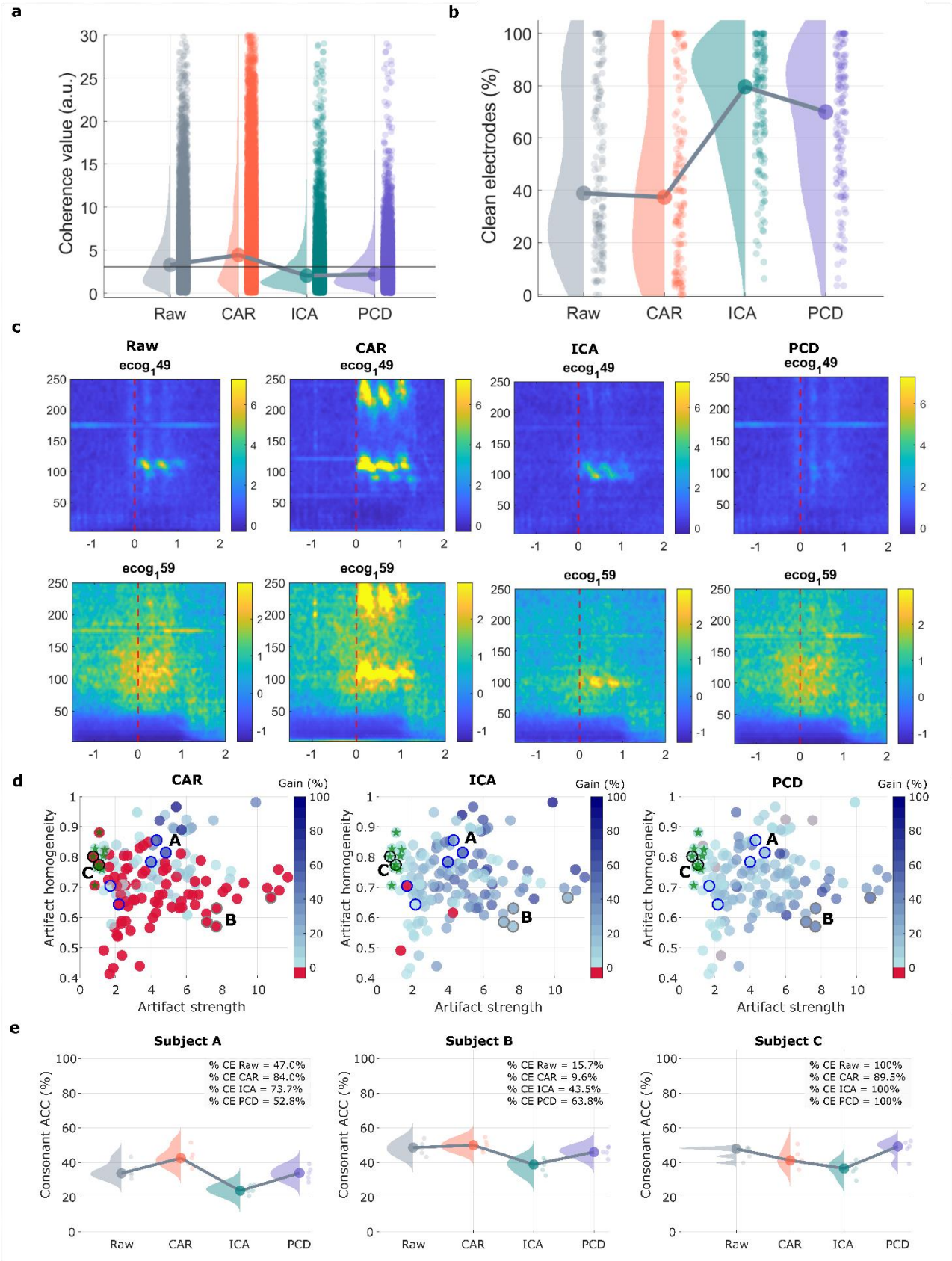

Fig. 5 | PCD removes the vibration artifact while preserving underlying γ-activity in intracranial recordings. **a**, Coherence value between a channel and the recorded audio, measured by means of ITPC. Here a dot represents a channel **b**, Percentage of clean electrodes, where every dot represents the data from a recording session. The horizontal solid line indicates the significance threshold. **c**, Time-frequency plots for raw signals and effect of applying each denoising method

in an electrode with strong vibration artifact (top row) and an electrode with physiological speech-related γ-activity (bottom row). **d**, Percentage gain in clean electrodes (Gain) versus artifact homogeneity and strength, for CAR, ICA, and PCD. Each dot represents the data from a recording session. Raw data with no detectable vibration artifact is marked with a green star. Data from 3 subjects (A, B and C) are highlighted: Homogenous artifact case (Subject A); Strong artifact case (Subject B) and No artifact case (Subject C) represented as circles with blue, gray and black contours, respectively. **e**, Impact in speech decoding from neural data (detection of consonant-vowel syllables) in three cases: i) clean electrode (CE) gain is higher for CAR and ICA than PCD (Subject A), ii) CE gain is better with PCD than for the other two methods (Subject B), and iii) data without vibration artifact (Subject C). ACC stands for accuracy, i.e., the number of correct classified samples over the total of samples. Every point shows the ACC for the deep learning architecture evaluated at given randomly assigned 5 initialization values of the trainable parameters (weights initialization).

Discussion

The head frame used in stereotactic neurosurgery introduces acoustic-induced vibrations that affect the quality of iEEG signals recorded intraoperatively during speech production. This recently described acoustic-induced artifact[8,9] overlaps in time and frequency with gamma-band activity, potentially compromising the reliability of speech-related analyses, including those used in BCI development. In this technical report, we demonstrated why traditional spatial filtering approaches are not appropriate for denoising the vibration artifact (Fig. 4-5). Specifically, we showed that CAR exacerbates the presence of the vibration artifact when it is heterogeneous across recording channels, subtracting the artifact to otherwise unaffected channels (Fig. 5 - CAR). Although ICA reduces the coherence of neural signals with the audio (Fig. 5a - ICA), this comes at the cost of a strong degradation of physiological γ-band modulations (Fig. 5c - ICA), which ultimately results in a reduction of speech-decoding performance from neural data (Fig. 5e - ICA).

In recent years, data-driven spatial filtering methods have been introduced as re-referencing schemes[11,14,24]. Such is the case of SSD, an effective method to increase the SNR for narrow-band, in which not only the central frequency of the band of interest is enhanced but also its harmonics[11]; a characteristic that is particularly suitable for denoising speech-induced vibration artifacts. Given that acoustic contaminations can be assessed by means of coherence with audio channels (ITPC)[8], PCO (another data-driven spatial-filtering method) is ideally suited to decompose the acoustic artifact source from brain recordings. By combining these methods, we developed PCD, a novel data-driven algorithm for denoising brain recordings contaminated with acoustic-induced artifacts (Fig. 1, Fig.2, Extended Data Fig. 1). Here, we show that PCD can retrieve the vibration artifact while preserving physiological γ-band modulations at overlapping frequencies (Fig. 3-4). Through extensive simulations we show that PCD works for different number of channels (from 3 to 100), different ratios of artifact to neural sources amplitude (from -100 to 30 dB), and across different durations of simulated artifact (from 0.5 to 3.5 s), although it is sensitive to the SSD filter parameters like the bandwidth around F0 (ΔF) and the filter order (Extended Data Fig. 4 and Supplementary Fig. 3).

The PCD method has several underlying assumptions. First, it assumes the vibration artifact is a narrow-band component around the fundamental frequency of the participant's voice, which must be estimated for each participant from audio recordings. Second, it assumes the artifact source is common across electrode modalities, thus allowing the combination of all recording modalities which maximizes the chance of extracting the artifact source[25]. While this might be counterintuitive, the artifact is likely due to mechanical vibrations of cables and connectors along the recording chain[9] which can affect different recording modalities in the same way. Third, we assume that the recorded audio is a good estimation of the true artifactual source (i.e., there is no spectral distortion or delay between audio and artifact). While this is a strong assumption, currently there is no better proxy for the artifactual source than the recorded audio. Violations of this assumption may explain the difference between simulated (Fig. 3-4) and real data performance (Fig. 5).

The current implementation of PCD has several limitations. (i) Performance declines for broadband artifactual sources (Extended Data Fig. 4), a limitation inherited from SSD, which is able to enhance the power only in narrow frequency bands[11,21]. This limitation could also partially explain the differences in performance between simulated and real data. (ii) The method does not account for systematic distortions between the recorded audio and the vibration artifact. Modelling such distortions might be a promising approach to further improve the method's performance in future studies. (iii) PCD is computationally expensive given that it involves solving a non-convex optimization problem, thus requiring several runs until selecting the best solution[22]. As such, PCD for online BCI applications would require further ad-hoc implementations to speed up the optimization process. (iv) The method

must be applied in a trial-wise manner given that the artifact's phase-relationship to the audio strongly varies across trials (Supplementary Fig. 9). For this reason, the method was fitted to individual speech production epochs to optimally estimate the artifact and then a wider window was applied to avoid introducing discontinuities that could affect subsequent analyses. Applying PCD per trial has the additional advantage of reducing memory requirements and computational cost.

Despite the orders of magnitude greater resolution of intracranial recordings compared to scalp EEG signals, induced vibration artifacts remain an important confound in the study of the neural control of speech production[8,9]. Critical to BCI development using intracranial recordings from overt speech production is the recognition that these artifacts can hamper training of robust machine learning models, which may be biased and fail when used for speech-impaired patients in real-life applications. Signal preprocessing should verify not only that artifactual components are removed or attenuated, but also that neural signals are retained. The PCD method may facilitate the building of BCI decoding models upon reliable neural data by avoiding artifactually driven performance. Additionally, PCD was designed specifically to mitigate loss of signal quality we observed using standard pre-processing methodologies for vibration artifact denoising. Using simulated data, we showed that when PCD's assumptions are satisfied, the method can completely remove the vibration artifact while preserving speech-related γ-band modulations. For real data, for which the underlying assumptions might not be strictly satisfied, PCD still achieves significant reductions of the strength and extent of the vibration artifact. The consonant decoder results obtained with PCD-denoised signals illustrate the practicability of this method for potential improvements in the reliability of BCI frameworks. Moreover, although this study focused on denoising acoustic-induced artifacts in intracranial recordings collected intraoperatively, PCD can be used to remove any narrow-band artifact from electrophysiological data, for which an estimate of the source is available.

References

1. Tekriwal, A., Felsen, G. & Thompson, J. A. Modular auditory decision-making behavioral task designed for intraoperative use in humans. *J Neurosci Methods* **304**, 162–167 (2018).
2. Lipski, W. J. *et al.* Subthalamic nucleus neurons differentially encode early and late aspects of speech production. *Journal of Neuroscience* **38**, 5620–5631 (2018).
3. Ma, J. *et al.* A large EEG dataset for studying cross-session variability in motor imagery brain-computer interface. *Sci Data* **9**, 1–9 (2022).
4. Moses, D. A. *et al.* Neuroprosthesis for decoding speech in a paralyzed person with anarthria. *New England Journal of Medicine* **385**, 217–227 (2021).
5. Proix, T. *et al.* Imagined speech can be decoded from low- and cross-frequency intracranial EEG features. *Nat Commun* **13**, 48 (2022).
6. Angrick, M. *et al.* Speech synthesis from ECoG using densely connected 3D convolutional neural networks. *J Neural Eng* **16**, 36019 (2019).
7. Anumanchipalli, G. K., Chartier, J. & Chang, E. F. Speech synthesis from neural decoding of spoken sentences. *Nature* (2019) doi:10.1038/s41586-019-1119-1.
8. Bush, A. *et al.* Differentiation of speech-induced artifacts from physiological high gamma activity in intracranial recordings. *Neuroimage* **250**, (2022).
9. Roussel, P. *et al.* Observation and assessment of acoustic contamination of electrophysiological brain signals during speech production and sound perception. *J Neural Eng* **17**, (2020).
10. Sabbagh, D., Ablin, P., Varoquaux, G., Gramfort, A. & Engemann, D. A. Predictive regression modeling with MEG/EEG: from source power to signals and cognitive states. *Neuroimage* **222**, (2020).
11. Schaworonkow, N. & Voytek, B. Enhancing oscillations in intracranial electrophysiological recordings with datadriven spatial filters. *PLoS Comput Biol* **17**, 1–29 (2021).
12. Cohen, M. X. A tutorial on generalized eigendecomposition for denoising, contrast enhancement, and dimension reduction in multichannel electrophysiology. *Neuroimage* **247**, 1–48 (2022).
13. Liu, Y., Coon, W. G., de Pesters, A., Brunner, P. & Schalk, G. The effects of spatial filtering and artifacts on electrocorticographic signals. *J Neural Eng* **12**, (2015).
14. Cohen, M. X. Comparison of linear spatial filters for identifying oscillatory activity in multichannel data. *J Neurosci Methods* **278**, 1–12 (2017).
15. Haufe, S., Dähne, S. & Nikulin, V. v. Dimensionality reduction for the analysis of brain oscillations. *Neuroimage* **101**, 583–597 (2014).
16. Wallstrom, G. L., Kass, R. E., Miller, A., Cohn, J. F. & Fox, N. A. Automatic correction of ocular artifacts in the EEG: a comparison of regression-based and component-based methods. *International journal of psychophysiology* **53**, 105–119 (2004).
17. Schaworonkow, N. & Nikulin, V. v. Is sensor space analysis good enough? Spatial patterns as a tool for assessing spatial mixing of EEG/MEG rhythms. *Neuroimage* **253**, (2022).
18. Michelmann, S. *et al.* Data-driven re-referencing of intracranial EEG based on independent component analysis (ICA). *J Neurosci Methods* **307**, 125–137 (2018).
19. Mercier, M. R. *et al.* Advances in human intracranial electroencephalography research, guidelines and good practices. *Neuroimage* **260**, (2022).
20. Jung, T.-P. *et al.* Removing electroencephalographic artifacts by blind source separation. *Psychophysiology* **37**, 163–178 (2000).
21. Nikulin, V. v., Nolte, G. & Curio, G. A novel method for reliable and fast extraction of neuronal EEG/MEG oscillations on the basis of spatio-spectral decomposition. *Neuroimage* **55**, 1528–1535 (2011).
22. Waterstraat, G., Curio, G. & Nikulin, V. v. On optimal spatial filtering for the detection of phase coupling in multivariate neural recordings. *Neuroimage* **157**, 331–340 (2017).

23. Huang, G., Liu, Z., van der Maaten, L. & Weinberger, K. Q. Densely connected convolutional networks. in *Proceedings of the IEEE conference on computer vision and pattern recognition* 4700–4708 (2017).
24. de Cheveigné, A. ZapLine: A simple and effective method to remove power line artifacts. *Neuroimage* **207**, (2020).
25. Cohen, M. X. Comparison of linear spatial filters for identifying oscillatory activity in multichannel data. *J Neurosci Methods* **278**, 1–12 (2017).
26. Welch, P. The use of fast Fourier transform for the estimation of power spectra: a method based on time averaging over short, modified periodograms. *IEEE Transactions on audio and electroacoustics* **15**, 70–73 (1967).
27. Canolty, R. T. *et al.* High gamma power is phase-locked to theta oscillations in human neocortex. *Science (1979)* **313**, 1626–1628 (2006).
28. Dähne, S. *et al.* Finding brain oscillations with power dependencies in neuroimaging data. *Neuroimage* **96**, 334–348 (2014).
29. Buzsáki, G. & Wang, X.-J. Mechanisms of gamma oscillations. *Annu Rev Neurosci* **35**, 203 (2012).
30. Meneghetti, N. *et al.* Narrow and Broad γ Bands Process Complementary Visual Information in Mouse Primary Visual Cortex. *eNeuro* **8**, (2021).
31. Gerstner, W. & Kistler, W. M. *Spiking neuron models: Single neurons, populations, plasticity*. (Cambridge university press, 2002).
32. Cavallari, S., Panzeri, S. & Mazzoni, A. Comparison of the dynamics of neural interactions between current-based and conductance-based integrate-and-fire recurrent networks. *Front Neural Circuits* **8**, 12 (2014).
33. Brunel, N. & Wang, X.-J. What determines the frequency of fast network oscillations with irregular neural discharges? I. Synaptic dynamics and excitation-inhibition balance. *J Neurophysiol* **90**, 415–430 (2003).
34. Mazzoni, A. *et al.* Computing the local field potential (LFP) from integrate-and-fire network models. *PLoS Comput Biol* **11**, e1004584 (2015).
35. Miller, K. J., Sorensen, L. B., Ojemann, J. G. & den Nijs, M. Power-law scaling in the brain surface electric potential. *PLoS Comput Biol* **5**, e1000609 (2009).
36. Mazzoni, A., Panzeri, S., Logothetis, N. K. & Brunel, N. Encoding of naturalistic stimuli by local field potential spectra in networks of excitatory and inhibitory neurons. *PLoS Comput Biol* **4**, e1000239 (2008).
37. Chrabaszcz, A. *et al.* Simultaneously recorded subthalamic and cortical LFPs reveal different lexicality effects during reading aloud. *J Neurolinguistics* **60**, 101019 (2021).
38. Chrabaszcz, A. *et al.* Subthalamic nucleus and sensorimotor cortex activity during speech production. *Journal of Neuroscience* **39**, 2698–2708 (2019).
39. Fischer, P. *et al.* Movement-related coupling of human subthalamic nucleus spikes to cortical gamma. *Elife* **9**, e51956 (2020).
40. Oostenveld, R., Fries, P., Maris, E. & Schoffelen, J.-M. FieldTrip: Open Source Software for Advanced Analysis of MEG, EEG, and Invasive Electrophysiological Data. *Comput Intell Neurosci* **2011**, 156869 (2011).
41. Gao, P. *et al.* A theory of multineuronal dimensionality, dynamics and measurement. *BioRxiv* 214262 (2017).
42. Cunningham, J. P. & Byron, M. Y. Dimensionality reduction for large-scale neural recordings. *Nat Neurosci* **17**, 1500–1509 (2014).
43. Chung, S. & Abbott, L. F. Neural population geometry: An approach for understanding biological and artificial neural networks. *Curr Opin Neurobiol* **70**, 137–144 (2021).

44. Koay, S. A., Charles, A. S., Thiberge, S. Y., Brody, C. D. & Tank, D. W. Sequential and efficient neural-population coding of complex task information. *Neuron* **110**, 328-349.e11 (2022).
45. Cohen, M. X. *Analyzing Neural Time Series Data: Theory and Practice*. (MIT Press, 2014).
46. Umakantha, A. *et al.* Bridging neuronal correlations and dimensionality reduction. *Neuron* **109**, 2740–2754 (2021).
47. Hermansky, H. Perceptual linear predictive (PLP) analysis of speech. *J Acoust Soc Am* **87**, 1738–1752 (1990).
48. Ablin, P., Cardoso, J.-F. & Gramfort, A. Faster Independent Component Analysis by Preconditioning with Hessian Approximations. *IEEE Transactions on Signal Processing* **66**, 4040–4049 (2018).
49. Winkler, I., Debener, S., Müller, K.-R. & Tangermann, M. On the Influence of High-Pass Filtering on ICA-Based Artifact Reduction in EEG-ERP. in *Proceedings of EMBC-2015* 4101–4105 (IEEE, 2015). doi:10.1109/EMBC.2015.7319296.
50. Berens, P. CircStat: a MATLAB toolbox for circular statistics. *J Stat Softw* **31**, 1–21 (2009).
51. Allen, M. *et al.* Raincloud plots: a multi-platform tool for robust data visualization [version 2; peer review: 2 approved]. *Wellcome Open Res* **4**, (2021).

Methods

The phase coupling decomposition algorithm

In the following, we denote the multivariate neuronal measurement acquired using electrocorticography (ECoG), LFP either from the macro ring on the shaft of the microelectrodes, the tip contact of the microelectrodes or the DBS lead, by the matrix $\boldsymbol{X} \in R^{N_c \times N_s}$, where N_c an N_s represent the number of channels and sample points, respectively. The acoustic signal associated to the vibration artifact is denoted by vector $\boldsymbol{z} \in R^{N_s}$. The phase coupling decomposition algorithm (PCD) seeks to find those artifactual sources by solving the inverse problem related to (1) so that each source can be estimated by:

$$\widehat{\boldsymbol{S}} = \boldsymbol{W}_{PCD}^{T}\boldsymbol{X}, \qquad (2)$$

where T denotes transpose (see Box 1). It can be thought of as a supervised two-step spatial filtering procedure which denoises based on low-rank factorization[15]. As shown in Box 1, the vibration artifact rejection comprises four main steps: 1) band-width estimation, 2) spatio-spectral decomposition, 3) phase-coupling optimization and 4) signal reconstruction. In the following, each step will be described.

1) Vibration artifact band-width estimation

The vibration artifact is a narrow-band component noise. It happens around the fundamental frequency (F0) of the participant voice[8]. The recorded audio signal $\boldsymbol{z}$, is used as a proxy for the vibration artifact frequency band estimation. We use Welch's method[26] for calculating the power spectra of the audio (detrended signal). An estimate of F0 from audio recordings is used as a starting point to find a peak in gamma band (50-250 Hz). The Gaussian curve fitting algorithm is used to calculate the central frequency (F_C) and band width (ΔF_c) of the vibration artifact frequency band (VAFB) by estimating the mean and full width at half maximum of the resulted fitted signal. The VAFB is then defined as $F_c \pm \Delta F_c$.

2) Spatio-spectral decomposition

The spatio-spectral decomposition algorithm (SSD) is a spatial filtering approach that allows to maximize the signal power at a given frequency peak while minimizing it for surrounding frequencies[21]. The method assumes that the recorded brain activity is a superposition of narrow band oscillations at the given frequency peak of interest (*signal*) and neighboring frequency bands (*noise*), that is $\boldsymbol{X} = \boldsymbol{X}_{signal} + \boldsymbol{X}_{noise}$. By traditional temporal filters, such as the Butterworth zero-phase filter, the signal and noise contributions to $\boldsymbol{X}$ can be separated[21].

The objective of SSD is to find a set of spatial filters (columns of an unmixing matrix $\mathbf{W}_{SSD}$) such that the power of the signal is maximized while the power of the noise is minimized:

$$\boldsymbol{w} = argmax_{\boldsymbol{w} \in \mathbb{R}^{N_C}} \frac{\boldsymbol{w}^T \Sigma_{\text{signal}} \boldsymbol{w}}{\boldsymbol{w}^T \Sigma_{\text{noise}} \boldsymbol{w}}, \qquad (3)$$

where $\Sigma_{\text{signal}} = \boldsymbol{X}_{signal}^{T}\boldsymbol{X}_{signal}$ and $\Sigma_{\text{noise}} = \boldsymbol{X}_{noise}^{T}\boldsymbol{X}_{noise}$ are the covariance matrices on the *signal band* and *noise band*, respectively.

The number of components returned by SSD is equal to the number of channels given in $\boldsymbol{X}$**,** sorted according to the relative power spectrum in the frequency band of interest. Using the first k SSD components, dimensionality reduction can be achieved by projecting the data on the reduced SSD space as follows:

$$\widetilde{\boldsymbol{X}}_{SSD} = \widetilde{\boldsymbol{W}}_{SSD}^{T}\boldsymbol{X}\ , \qquad (4)$$

where $\widetilde{\boldsymbol{W}}_{SSD} = [\boldsymbol{w_1}, \dots, \boldsymbol{w_k}]$.

In the context of the vibration artifact denoising we consider here that our frequency band of interest is the VAFB. Also, the data projected on the first k SSD components $\widetilde{\boldsymbol{X}}_{\boldsymbol{SSD}}$ is used as the starting point to run the second spatial filtering technique involved in the PCD pipeline.

3) Phase-coupling optimization

Phase-coupling optimization (PCO) is a supervised spatial filtering algorithm developed by Waterstraat et al. that seeks to recover neural sources that are phase-coupled to an external target variable[22]. The optimization criterion is based on the maximization of the mean vector length[27] (MVL), a differentiable metric that results in values different from zero when a phase coupling exists. Within this denoising pipeline, we take advantage of the PCO formulation and extend it in order to find the artifactual sources underlying neural activity. Phase coupling is then computed via the MVL between the SSD data projection $\widetilde{\boldsymbol{X}}_{\boldsymbol{SSD}}$ and the best guess of the artifact source. Considering that data in SSD space belong to the complex domain, the analytic signal $\boldsymbol{Y}_{SSD} \in \mathbb{C}$ should be first obtained. The Hilbert transform is utilized to find the imaginary part such that:

$$\boldsymbol{Y}_{SSD} = \boldsymbol{X}_{SSD} + i\mathcal{H}(\boldsymbol{X}_{SSD}) \in \mathbb{C}, \tag{5}$$

where i denotes the imaginary unit defined so as $i^2 = -1$.
Therefore, the MVL is defined by:

$$MVL = \left| \frac{1}{N_S} \sum_{\mathrm{t}=1}^{N_S} \frac{z_t \boldsymbol{w}^T \boldsymbol{y}_t}{|\boldsymbol{w}^T \boldsymbol{y}_t|} \right|. \tag{6}$$

Assuming that the artifact source is the recorded audio signal $\boldsymbol{z}$, a linear filter $\boldsymbol{w}_{PCO} = \boldsymbol{w} = [w_1, \dots, w_k]$ is found by maximizing the mean vector length at each sample point between the acoustic signal and the SSD components, as follows:

$$\mathbf{w}_{PCO} = argmax_{\mathbf{w}_{PCO} \in \mathbb{R}^k} \left| \frac{1}{N_S} \sum_{\mathrm{t}=1}^{N_S} \frac{z_t \boldsymbol{w}^T \boldsymbol{y}_t}{|\boldsymbol{w}^T \boldsymbol{y}_t|} \right|, \tag{7}$$

where $|\cdot|$ denotes the amplitude of a complex signal and $\boldsymbol{y}_t$ is $k-$ dimensional vector at the $t^{th}-$ sample point.

Although the function defined in (7) is differentiable, convexity with respect to $\boldsymbol{w}$ cannot be guaranteed. Thus, the best solution is selected out of a pool of different solutions found by several random initializations of $\boldsymbol{w}$. Typically, between 10 and 15 independent runs of the algorithm are done, and the solution with the largest MVL is selected as the best one. The complete set of spatial filters that defines the PCO demixing matrix $\boldsymbol{W}_{PCO} \in \mathbb{R}^{k \times k}$ is found by solving (7) iteratively, outprojecting the previously found filters from the solution space[22,28], in which data was firstly whitened by a matrix $\boldsymbol{M}$. The column vectors of $\boldsymbol{W}_{PCO}$ are sorted in decreasing order according to the MVL value found during the optimization procedure. Thus, the first m components from the resulting data projection in the PCO space $\boldsymbol{X}_{PCO} = \boldsymbol{W}_{PCO}^{\boldsymbol{T}} \boldsymbol{X}_{SSD}$ correspond to the vibration artifact sources.

4) Signal reconstruction

The objective of the PCD pipeline is to denoise signals contaminated with the vibration artifact. The artifact source estimation is just a proxy to facilitate data cleaning. Given that two spatial filtering transformations are applied as a chained process, the PCD unmixing matrix $\boldsymbol{W}_{PCD}$ which project the raw data from the amplifier space to the artifact source space should be computed by taking into account the learned linear transformations $\boldsymbol{W}_{PCO}$ and $\boldsymbol{W}_{SSD}$ as follows:

$$\boldsymbol{W}_{PCD} = \boldsymbol{M}\,\boldsymbol{W}_{SSD}\begin{bmatrix}\boldsymbol{W}_{PCO} & \boldsymbol{0} \\ \boldsymbol{0} & \boldsymbol{I}_{(N_c-k\times N_c-k)}\end{bmatrix}, \tag{8}$$

where $\boldsymbol{I}$ denotes the identity matrix of dimension $N_c - k \times N_c - k$, and $\boldsymbol{M}$ is the $N_c \times N_c$ whitening matrix applied to find the set of solution vectors to (7).

Once the unmixing matrix is computed, the mixing matrix that defines the forward model explained in (1) can be calculated based on its pseudoinverse:

$$\boldsymbol{A}_{PCD} = \boldsymbol{W}_{PCD}^{\dagger},$$

where † denotes the Moore–Penrose pseudoinverse. Then the set of equations that define the linear forward and backward model is given by:

$$\begin{cases}\boldsymbol{X} = \boldsymbol{A}_{PCD}\boldsymbol{S} \\ \widehat{\boldsymbol{S}} = \boldsymbol{W}_{PCD}^{\boldsymbol{T}}\boldsymbol{X}\end{cases}$$

Now, by low-rank factorization the denoised signal can be reconstructed by zeroing from the mixing and unmixing matrix the first m components which were previously identified as artifactual. Thus, signal reconstruction is simply done by:

$$\boldsymbol{X}_{denoised} = \widetilde{\boldsymbol{A}}_{PCD}\widetilde{\boldsymbol{W}}_{PCD}^{\boldsymbol{T}}\boldsymbol{X},$$

where $\widetilde{\boldsymbol{A}}_{PCD}$ and $\widetilde{\boldsymbol{W}}_{PCD}$ represents the mixing and unmixing matrices of rank $N_c - m$, respectively.

Simulated Neural Data

Description of the neural source model

We simulated a recurrent network of leaky integrate-and-fire (LIF) neurons (N = 5000): 80% excitatory neurons I with AMPA-like synapses and 20% inhibitory neurons (I) with GABA-like synapses[29,30] (Extended Data Fig 2, Supplementary Table 1 for parameters). The connectivity architecture is sparse and random with an average connection probability between any pair of cells of 0.2.

The membrane potential V^I of each neuron i evolves according to the following dynamics[31]:

$$\tau_m^i \frac{dV(t)^i}{dt} = -V(t)^i + V_{leak}^i - R_m I(t)_{tot}^i$$

where τ_m is the membrane time constant, V_{leak} is the leak membrane potential, R_m is the membrane resistance and $I(t)_{tot}$ is the total input current. The neuron triggers a spike at time t^* if $V(t^*) \geq V_{thr}$ where V_{thr} is the threshold potential. Then, the membrane voltage is set to the reset membrane potential $V_{reset}$for the duration of the absolute refractory time period Δ.

We broke down the term $I(t)_{tot}$ into two distinct contributions, namely the sum of all the current-based synaptic inputs entering the $i - th$ neuron $I(t)_{syn}$ and the external current input $I(t)_{ext}$, as follows:

$$I(t)_{tot}^i = I(t)_{syn}^i + I(t)_{ext}^i = \sum_{j\in E} J^{j\to i}\,\mathrm{S(t)}_{\mathrm{AMPA}}^{\mathrm{j}} + \sum_{k\in I} J^{k\to i}\,\mathrm{S(t)}_{\mathrm{GABA}}^{\mathrm{k}} + I(t)_{ext}$$

where $J^{j,k\to i}$ is the efficacy of the synapsis that connects the $j,k-th$pre-synaptic neuron to the $i-th$ post-synaptic neuron. $\mathrm{S(t)}_{\mathrm{syn}}^{\mathrm{j,k}}$ represents the synaptic dynamics which primarily depends on the synapsis type $E{:}\,AMPA, I{:}\,GABA$[32]. Every time a $j,k-th$ presynaptic neuron fires at time t^*, $\mathrm{S(t)}_{\mathrm{syn}}^{\mathrm{j,k}}$ is increased by an amount described by a delayed difference of exponentials, as follows:

$$\mathrm{S(t)}_{\mathrm{syn}}^{\mathrm{j,k}} = \mathrm{S(t)}_{\mathrm{syn}}^{\mathrm{j,k}} + \Delta S(t)$$

$$\Delta S(t) = \frac{\tau_m}{\tau_d - \tau_r}\left(e^{-\frac{t-t^*-d}{\tau_d}} - e^{-\frac{t-t^*-d}{\tau_r}}\right),$$

where τ_r is the rise time, τ_d is the decay time and d is the latency of the synapsis[33]. We defined γ-source activity as the proxy of the local field potential computed by summing the absolute values of the excitatory and inhibitory currents entering the E population[34].

External input into the neural source model

Both populations (excitatory and inhibitory units) receive a time-varying stochastic external current input $I(t)_{ext}$ that represents the background activity from external (e.g., thalamocortical) afferents, with I neurons receiving more efficacious synapses than E neurons (Supplementary Table 1). The external input was implemented as a series of Poissonian inputs to excitatory synapses with similar kinetics to the recurrent AMPA synapses, but with different efficacy (Supplementary Table 1). These synapses were excited by independent realizations of the same Poissonian process with time-varying input rate $\nu_{ext}(t)$, and therefore, contributing to the single-neuron variability. The $\nu_{ext}(t)$ was composed of the superposition of the signal term $\nu_{signal}(t)$ and the noise term $\zeta(t)$ as follows:

$$\nu_{ext}(t) = \lfloor \nu_{signal}(t) + \zeta(\mathrm{t}) \rfloor_+$$

where $\lfloor\cdot\rfloor_+$ is the positive part operator.

We modelled the noise component of the input rate $\zeta(t)$ as a zero-mean Ornstein-Uhlenbeck (OU) process, as follows:

$$\tau_\zeta \frac{\mathrm{d}\,\zeta(t)}{\mathrm{dt}} = -\,\zeta(t) + \sigma_\zeta\left(\sqrt{2\tau_\zeta}\right)\eta(\mathrm{t}),$$

where $\eta(t)$ is the realization of a Gaussian white noise and σ_ζ, τ_ζ are the standard deviation and the time constant of the OU process, respectively. τ_ζ was set to have a knee in the OU power spectrum at 10 Hz [35].

Essential dynamics properties of the source activity

We validated essential properties - which have been already extensively investigated elsewhere[33,36] - of the neural dynamics network with different expressions for $\nu_{signal}(t)$: sustained signals, periodically modulated signals and signals modulated with a Gaussian profile (Extended Data Fig. 4).

First, we modeled external sources with sustained rate with amplitude varying between 2 and 20 spikes/ms. The reverberance of the E-I recurrent connections favored the emergence of reliable broadband γ-oscillations in the [60-150] Hz range (Extended Data Fig. 4). These γ-oscillations encoded the sustained signal increasing the power as the amplitude of the signal increases. It is

noteworthy that this frequency range is compatible with the high-gamma speech-related spectral modulation shown in the literature[5,7,37].

Second, we modeled external inputs with a periodically modulated firing rate, with a varying modulation frequency between 5 and 20 Hz. The source entrained the signal fluctuations generating phase-locked oscillations at the same frequency of the periodic modulation of external input. When a superposition of the sustained and periodic signal was fed into the source, we observed the emergence of two spectral information channels: γ-oscillations that track the mean rate of the signal and low-frequency oscillations entrained by the slow time-scale component in the signal. Interestingly, the phase of the low-frequency oscillations was strongly coupled with the amplitude of γ-oscillations with surges of γ-power close to the peak of the low-frequency oscillation ($\sim \pi/8$ phase) (Supplementary Fig. 1)

Finally, to reproduce the temporal pattern of the γ-source activity, e.g., event-locked transient synchronization, we fed gaussian-modulated input rates of external signals in the model (Extended Data Fig. 2, Supplementary Fig. 6). The time-activation parameters of the gaussian signal (i.e., fullwidth at half maximum and mean) regulated the duration and temporal focality of the broadband γ-source synchronization (Supplementary Fig. 6).

Linear mixing of neural and audio sources

We simulated 99 neural γ-sources and one audio source $\mathcal{S}_a$ for each simulation. Different sources were fed by different realizations of the $\nu_{signal}(t)$ which expression depends on the simulation scenario (see below and Supplementary Table 1). Therefore, most of the variability at the source-level owes to the stochasticity in $\nu_{signal}(t)$.

In simulation settings we assumed that:

1. One source owes the major contribution to the acoustic-induced artifact ($m = 1$).
2. The audio signal $\boldsymbol{z} = z(t)$ used during the denoising pipeline is a good approximation of the artifact source $\left(\mathcal{S}_a(t) \approx z(t)\right)$, i.e., the transfer function from audio signal to vibration artifact is the identity.
3. The mixing matrix A is square.

70% of γ-sources were fed by non-null $\nu_{signal}(t)$ and, as such was considered as "active". To impose the artifact-to-physiological gamma ratio (AGR), we adjusted the scale of the neural γ-sources by applying a correction factor κ, such that:

$$\kappa = \frac{\gamma_a}{\gamma_n} 10^{-AGR/10},$$

where γ_a and γ_n are the power of the audio source and neural sources in the [70-180] Hz frequency range, respectively.

We projected the neural γ-sources and the artifact source into the amplifier space $\boldsymbol{X}$ applying a random mixing matrix A. We included inter-trial variability sampling A at each simulation. By imposing the non-singularity of A, we avoided ill-posed inversion problems.
Ground truth data $\boldsymbol{X}_{gt}$, i.e., noiseless data, were generated by removing the audio source in the mixing operation.

Simulation scenarios

The $\nu_{signal}(t)$ expression and the procedure used to synthesize the audio source delineated the different simulation scenarios considered in this work, as depicted by Extended Data Fig 2.

Toy examples

We used toy examples for initial assessment of the effect of the PCD pipeline to remove the acoustic-induced artifact in *in-silico* neural signals. We used three scenarios for these toy examples, where $\nu_{signal}(t)$ was defined as the superposition of the sustained and periodically modulated signal, as follows:

$$\nu_{signal}(t) = A_s + A_p \sin\left(2\pi f_p t + \varphi_p\right),$$

where A_s is the amplitude of the sustained input, and A_p, f_p and φ_p are the amplitude, the frequency and the phase of the periodic signal, respectively.

In Scenario 1 (Sinusoidal audio scenario, SAS), we synthetized the contaminating audio source $\mathcal{S}_a$ as a sinusoidal function with noise, as follows:

$$\mathcal{S}_a(t) = A_0 sin(2\pi F_0 t + \varphi_0) + \eta(t),$$

where A_0 is the amplitude, F_0 is the fundamental frequency, φ_0 is the phase, and $\eta(t)$ is the white noise term.

In Scenario 2 (Colored noise audio scenario, CAS), the audio source was synthesized by coloring the spectrum of the white noise $\eta(t)$, as follows:

$$\mathcal{S}_a(t) = BP(t) * \sigma\eta(t),$$

where BP(t) is the impulse response of the 25th order Butterworth filter, σ is the standard deviation and $*$ is the convolution operator.

In Scenario 3 (Modulated colored noise scenario, MCAS), we mimicked the temporal profile of the audio in the Syllable Repetition Task (see *Triplet repetition task data*), applying the activation pattern $M(t)$ to the audio source in Scenario 2, which reads:

$$M(t) = \begin{cases} 1, & t_i < t < t_i + 0.5 \\ 0, & elsewhere \end{cases}; i = 1,2,3$$

where t_i is the onset of $i - th$ syllable, which lasts 0.5 s.

Realistic scenario

In this Scenario (recorded audio scenario, RAS), we simulated 60 trials of speech-locked transient γ-source activity, feeding Gaussian signals in the network, as follows:

$$\nu_{signal}(t) = \mathrm{A}e^{-\frac{(t-\mu)^2}{\left({}^{2\mathrm{FWHM}}/_{2.355}\right)^2}},$$

where A and μ are the intensity and temporal location modulation, and $FWHM$ is the fullwidth at half maximum which controls the temporal focality of the modulation. Parameters were set to reproduce physiological speech-locked γ-modulation patterns described in literature[4,38,39]. As audio source, we selected the recorded audio signals during the Syllable Repetition Task with different audio spectrogram profiles, e.g., non-stationary pitch (Supplementary Fig. 7).

Computational simulation settings

The simulations were performed using a finite difference integration scheme based on the 2nd-order Runge-Kutta algorithm with discretization time step $\Delta t = 0.05\, ms$. to update the neural dynamics. Simulation duration varied between 1 s and 10 s. We did not include the first 200 ms of each simulation in the analysis to avoid transitory dynamics in the network. We fixed the seeds of the random generator number for sake of the reproducibility across different simulation sessions.

Triplet repetition task data

54 English-speaking patients undergoing an awake DBS implantation surgery consented to participate in an intraoperative speech task at the University of Pittsburgh (IRB Protocol #PRO13110420). Patients were instructed to repeat consonant-vowel syllable triplets that were played on their earphones. Specifically, the basis set of phonemes included 4 consonants (/v/, /t/, /s/, /g/) and 3 cardinal vowels (/i/, /a, /u/) with distinctive tongue positions and acoustic properties. 1 to 4 recording sessions of up to 120 syllable triplets each were performed by participants. Sessions differed regarding the neural recording modalities registered. Electrocorticography (ECoG) was always registered through one or two strips of 53 or 64 contacts targeted to cover the left ventral sensorimotor cortex, superior temporal gyrus and inferior frontal regions. MER and LFPs from a macro ring located 3mm above the microelectrode tip were registered during subcortical target mapping, for participants undergoing subthalamic nucleus (STN) or Globus Pallidus Internus (GPi) DBS. LFP registered from the DBS lead were recorded from the STN, GPi and ventral intermediate nucleus (VIM). The produced audio signal was recorded by a directional microphone placed near the patient's mouth. Data was time-aligned, pre-processed, low-pass filtered at 500Hz, down-sampled to 1kHz and saved as a FieldTrip[40] object for subsequent analyses. For more information about the dataset, we refer the reader to Bush et al. 2021[8].

Algorithm implementation

Trial-wise denoising

Since phase relationships between the artifact source and the neural recordings is not consistent across trials (Supplementary Fig. 9), the PCD pipeline was applied on a trial-wise basis. Data was high-pass filtered above 2 Hz and notch-filtered at 60 Hz and its three first harmonics. Given that the artifact was observed only during overt speech production times, epochs around the produced speech onset were extracted for fitting the model. Under the hypothesis that the artifact is introduced in the acquisition chain, the different synchronized brain recording modalities (MER-LFP + ECoG or DBS-LFP + ECoG) were combined to form a unique data matrix. That is, the signals from all available brain recording modalities were treated as a unique sensor space.

For every trial, the model was fitted as follows. First, the epoched audio signal was used to estimate the VAFB, and thus the noise and signal band were accordingly defined (Box 1 - step 1, Extended Data Fig. 1, Methods). Data preparation proceeded, which included applying the Hilbert transform to find the analytic representation of the signal, as well as data whitening. The audio signal was z-scored for normalization purposes and used as the best guess of the artifact source. The SSD algorithm was applied to the real part of the signal. The final number of SSD components to keep (k) was automatically selected based on the participation ratio (PR), defined as follows:

$$PR = \left\lfloor \frac{(\sum_i \lambda_i)^2}{\sum_i {\lambda_i}^2} \right\rfloor,$$

where $\lambda_1 \geq \lambda_2 \geq \cdots \geq \lambda_{N_C}$ are the eigenvalues resulting from solving SSD which account for the SNR participation of each SSD component. The PR has been shown to be a reasonable measure of neural dimensionality in PCA[41]. PCO was applied on data projected onto the SSD space, extracting one component at the time. Every component resulted in a mean vector length (MVL) value, such that $\mathrm{MVL}_1 \geq \mathrm{MVL}_2 \geq \cdots \geq \mathrm{MVL}_k$. Once both spatial filtering methods were learned, the unified unmixing and mixing matrix that described the PCD pipeline were computed (Box 1 – step 4, Methods).

The identification of the artifactual sources was also automatically done by finding the elbow in the trace of the MVL value across components, that is the point at maximum curvature differentiating the contribution of strong and weak components. Those components showing the highest MVL values were identified as artifactual.

Considering that further analysis would be done on the data, a wider epoch starting 6 seconds before and ending 6 seconds after the produced onset was used when applying the learned matrix transformation.

Algorithm stress test on simulated data: parametric sweep and performance evaluation
We applied the PCD pipeline on simulated data using the vibration artifact $\mathcal{S}_a(t)$ as audio signal $\left(\mathcal{S}_a(t) \approx z(t)\right)$. Because we simulated only one artifactual source, we expected the PCO to find only one component with high coherence with the audio (i.e. MVL) in the PCO space. To assess the performance of the denoising pipeline, we calculated time-, frequency- and phase-domain metrics that estimate the agreement between the ground-truth $\boldsymbol{X_{gt}}$ and cleaned data $\boldsymbol{X}$, and $z(t)$ and $z(t)_{est}$.

For each channel, we compared the similarity in the time-domain of the neural data $\left(\boldsymbol{X}\ vs.\boldsymbol{X_{gt}}\right)$, as follows:

$$\chi^2 = \frac{1}{T}\sum_t^T \frac{\left(\boldsymbol{X}-\boldsymbol{X}_{gt}\right)^2}{\sigma^2\left(\boldsymbol{X}_{gt}\right)}, \qquad (9)$$

where T is the duration of the simulation and $\sigma^2(\cdot)$ is the variance. χ values have been converted to a logarithmic scale for visualization purposes (Extended Data Fig. 4, Supplementary Fig. 3, Supplementary Fig. 5).

To assess the fidelity of the estimated speech-induced artifact $(\boldsymbol{z}\ vs.\tilde{\boldsymbol{z}})$, we used the magnitude coherence estimate (MSCE) and the consistency of the phase difference based on the PLV. The MSCE returns values between 0 and 1 indicating how similar two signals are at each frequency, as follows:

$$\mathrm{MSCE}(f) = \frac{\left|P_{\boldsymbol{z},\tilde{\boldsymbol{z}}}(f)\right|^2}{P_{\boldsymbol{z},\boldsymbol{z}}(f)P_{\tilde{\boldsymbol{z}},\tilde{\boldsymbol{z}}}(f)}, \qquad (10)$$

where P stands for the power spectral density. The PLV is a metric between 0 and 1 that quantifies the phase agreement between two signals, as follows:

$$PLV = \left|\sum_t^T \frac{e^{i(\phi_z(t)-\phi_{\tilde{z}}(t))}}{T}\right|, \qquad (11)$$

where ϕ is the instantaneous phase.

Moreover, to stress the PCD pipeline in the different scenarios, we evaluated performance during a sweep of key parameters, including the AGR [-100, 30] dB, $F0$ [70, 180] Hz and N_c [3, 100] in the SAS scenario. We swept ΔF $[2, 16]$ Hz, the filter order $[3, 27]$ and the simulation duration [0.5, 3.5] s in the CAS scenario.

Neural preservation assessment

Principal Component Analysis (PCA) is a dimensionality reduction technique that identifies an ordered set of orthogonal directions that captures the greatest variance in the data. It is widely accepted and used in the neuroscience community for analyzing neural population activity[42]. The low-dimensional space identified by PCA captures variance of all types, including noise. Such data representation can be thought of as the Cartesian coordinate basis describing subspaces in which the data lie[43]. Thus, for assessing neural preservation after applying denoising methods, the PCA low-dimensional space was utilized. Subspaces describing the same geometry as the ground truth data should be found after denoising if neural preservation is achieved. Thus, for every denoising pipeline, as well as the ground truth and the noisy data, PCA was fitted independently. The learned loading and scores were plotted for each decomposition made on the first 3 principal components (PC).

To quantify the degree of similarity between the PCA loadings ($\boldsymbol{L} \in \mathbb{R}^{N_c \times N_c}$) of the ground-truth data and the resulting data after each denoising pipeline was applied, the cosine similarity (CS)[44] was used. CS measures the extent to which two vectors point in the same direction. Given that PCA loading signs are arbitrary, bounded CS between 0 and 1 can be found by taking the absolute value of the cosine similarity, as follows:

$$CS_i = \left|\frac{\boldsymbol{L}_i^{gt}\boldsymbol{L}_i}{\left\|\boldsymbol{L}_i^{gt}\right\|\|\boldsymbol{L}_i\|}\right|, \qquad (12)$$

where i denotes the index of a given loading vector, $\boldsymbol{L_{gt}}$ indicates the PCA loading matrix of the ground-truth data $\boldsymbol{X_{gt}}$, $\boldsymbol{L}$ stands for the PCA loading matrix of a given denoised data $\boldsymbol{X}_{denoised}$, and $\|\cdot\|$ and $|\cdot|$ denotes the $\ell_2 -$ norm and the absolute value operators, respectively. The closer CS is to 1, the more similar the two vectors are. Thus, a good denoising pipeline from the neural data preservation point of view should be the one from which PCA loading vectors resemble the same directions (see Fig. 4d).

Inter-trial coherence for vibration artifact quantification

The vibration artifact level at each electrode was computed based on the inter-trial phase consistency (ITPC)[45], following the same framework proposed and used in Bush et al. 2021. That is, the audio and the neural signals were band-pass filtered between 70 and 240 Hz, i.e., within the plausible VAFB range. Then considering the complex representation of the neural data for a given channel $\boldsymbol{y} = \boldsymbol{x} + i\mathcal{H}(\boldsymbol{x})$ and the audio signal $\boldsymbol{z}$ at a given trial e, the phase between these two quantifies can be measured by:

$$\varphi_e = \frac{1}{\|\boldsymbol{y}\|\|\boldsymbol{z}\|}\sum_t y_t z_t.$$

At the end of this procedure, all the phases across the N_t trials are arranged on a vector $\boldsymbol{\varphi} = [\varphi_{\mathbf{1}}, \dots, \varphi_{\boldsymbol{N_t}}]$. If there is inter-trial phase consistency, the mean value of $\boldsymbol{\varphi}$ across trials ($\langle\boldsymbol{\varphi}\rangle$) will be different from 0, and thus it can be quantified as follows:

$$ITPC = \frac{|\langle\boldsymbol{\varphi}\rangle|}{std(\boldsymbol{\varphi})}, \qquad (13)$$

where $std(\cdot)$ stands for the stand deviation. It has been found that ITPC values equal or above 3.08[8] indicates that the presence of the vibration artifact on that given electrode is significant, and thus the electrode must be considered contaminated[8].

Artifact presence quantification: definition of homogeneity, strength and clean electrode gain
Artifact homogeneity should quantify the consistency of the artifact presence across electrodes. Let us denote $\boldsymbol{\vartheta} = [ITPC_1, \dots, ITPC_{N_C}]$ as a vector with the stored ITPC value found per each electrode. Considering that n −dimenstional unit vectors have variance between 0 and $1/n$, following the idea proposed by Umakantha et al.[46] we define the artifact homogeneity as follows:

$$artifact\ homogeneity = 1 - var(\frac{\boldsymbol{\vartheta}}{\|\boldsymbol{\vartheta}\|})N_c, \qquad (14)$$

that is, a value between 0 and 1, for homogeneous artifact presence and non-homogeneous artifact presence, respectively. Artifact strength was directly measure by the mean ITPC value found across electrodes:

$$artifact\ strength = mean(\boldsymbol{\vartheta}). \qquad (15)$$

The clean electrode gain was computed as the relative change of the clean electrode percentage before ($\%CE_{denoised}$) and after ($\%CE_{raw}$) applying a denoising method, that is:

$$gain = \%CE_{denoised} - \%CE_{raw}$$

Deep learning model for consonant identification
Densely-connected convolutional neural networks (DenseNet)[23] were trained to classify the consonants from neural signals (ECoG). For each syllable, original/denoised ECoG signals were spectrally filtered into 7 frequency bands ranging between 0 to 250 Hz. These syllable-level neural data were used as training set. We then extracted the perceptual linear prediction (PLP)[47] features from the corresponding audio recordings. Both PLP features and consonant identities were used as training labels. Our DenseNet model was designed to first map neural signals into PLP spectra and then predict the consonant class from the PLP space. For that purpose, the mean-squared-error loss of PLP feature prediction and the cross-entropy loss of consonant classification were jointly optimized during model training. We used 5-fold cross-validation while measuring model performance, withholding a different 20% partition from the training data as test set each time. Separate models were trained for each subject and each data type, resulting in 12 different models (3 subjects, 4 data types: Raw, CAR, ICA, PCD). During testing, reserved ECoG data were fed into the trained model, and the accuracy was measured based on the consonant predictions.

Traditional methods for denoising.

CAR as a spatial filtering algorithm

Common average reference (CAR) is a spatial filtering method that subtracts the common noise at every electrode, calculated as the average of all recordings. The data re-referenced via CAR is calculated as follows:

$$\begin{aligned} \boldsymbol{X}_{CAR} &= \boldsymbol{X} - \bar{\boldsymbol{X}} \\ &= \boldsymbol{X} - \frac{1}{N}\boldsymbol{J}\boldsymbol{X} \\ &= \left[\boldsymbol{I} - \frac{1}{N_c}\boldsymbol{J}\right]\boldsymbol{X} \\ &= \boldsymbol{W}_{CAR}\boldsymbol{X}, \end{aligned}$$

where N_c accounts for the number of electrodes and $\boldsymbol{J} = [\mathbf{1}^{N_c}]^T$ is an $N_c \times N_c$ matrix of ones. With this formulation it is easy to see that CAR can be thought of as a spatial filtering method which implies a linear transformation of the data.

Given that CAR takes the average across channels, data structure is not critical in this matter. The matrix transformation was applied in the continuous data for each type of channel recording.

The PCA + ICA pipeline

Independent component analysis (ICA) assumes that the sources linearly mixed in (1) are independent. Such an assumption is true for many artifacts that appear in brain recordings, like electrocardiography or electromyography. In order to ensure that independent sources are extracted from the data, non-gaussianity of $\boldsymbol{W}^T\boldsymbol{X}$ is maximized. Here in particular, ICA is implemented using Picard[48], a fast algorithm to solve the maximum likelihood estimation ICA formulation. This ICA implementation was chosen since it is known to result in robust components estimations in cases where the sources are not completely independent.

Basic data pre-processing was done before applying ICA. A temporal filtering above 2 Hz was implemented in order to remove low-frequency drifts, which can negatively affect the quality of the ICA fit[49]. Then data was z-scored and PCA was applied in order to both feed ICA with whitened data and to reduce the dimensionality of the problem. The number of PCA components was automatically selected by setting the explained variance to 0.99. As in the PCD pipeline, model fitting was done using the windowed data within the produced audio epoch, combining, if exists, the different brain recording modalities. For the sake of comparison with PCD, artifactual sources identification was done based on the circular mean of the phase difference. Those components showing the highest phase-locking values were selected as artifactual. Denoising via low-rank factorization was applied in the wider epochs, as done for PCD.

Computing environment

Data simulation and numerical experiments were conducted in Matlab 2020b. We used custom-based scripts (BML toolbox; https://github.com/Brain-Modulation-Lab/bmlbmlbmlbmlbml based on the Fieldtrip library (https://www.fieldtriptoolbox.org). We used online available implementations of SSD (https://github.com/svendaehne/matlab_SSD) and PCO (https://github.com/neurophysics/PCO_matlab). For measuring the phase-locking values and phase differences the CircStast toolbox (https://www.jstatsoft.org/article/view/v031i10) was utilized. In addition, Rstudio was used to compute the ITPC. For computing the simulations, we used the publicly available C-optimized implementation (http://senselab.med.yale.edu/ModelDB/ShowModel.asp?model=152539)[32]. We computed the

MSCE and the consistency of the phase difference by using the built-in MATLAB *mscohere* function and *circ_r* function in the CircStat Toolbox[50], respectively. We used the RainCloud library[51] to compare distributions of data (https://github.com/RainCloudPlots/RainCloudPlots#read-the-preprint).

Data availability

The data that support the findings of this study are available upon reasonable request. A formal data sharing agreement is required.

Code availability

The code for the PSD algorithm is available online at https://github.com/Brain-Modulation-Lab/PCD

Acknowledgements

We would like to thank research participants for their generous contribution of time and effort in the operating room and additional experimenters who acquired and organized the data. This work was funded by the National Institute of Health (BRAIN Initiative), through grants U01NS098969, U01NS117836 and R01NS110424 to R.M.R.

Author contributions

V.P., M.V. and A.B. conceived the computational experiments, and R.M.R conceived the experimental task design. V.P conceived and coded the initial algorithm. V.P and M.V designed the final algorithm and pipeline. A.B performed the data curation. M.V. designed and coded the simulated data framework. V.P. and M.V. tested the algorithm against real and simulated data. S.L. and Q.R. did the deep-learning experiments. V.P, M.V, S.L, Q.R. and A.B contributed tools to curate and analyze data. A.B., N.E.C and R.M.R gave insights into analyzing results. The original draft was written by V.P and M.V. and was revised and edited by all authors. R.M.R supervised the project.

Corresponding author

Correspondence to Alan Bush (alan.bush@mgh.harvard.edu)

Competing interests

The authors declare no competing interests.

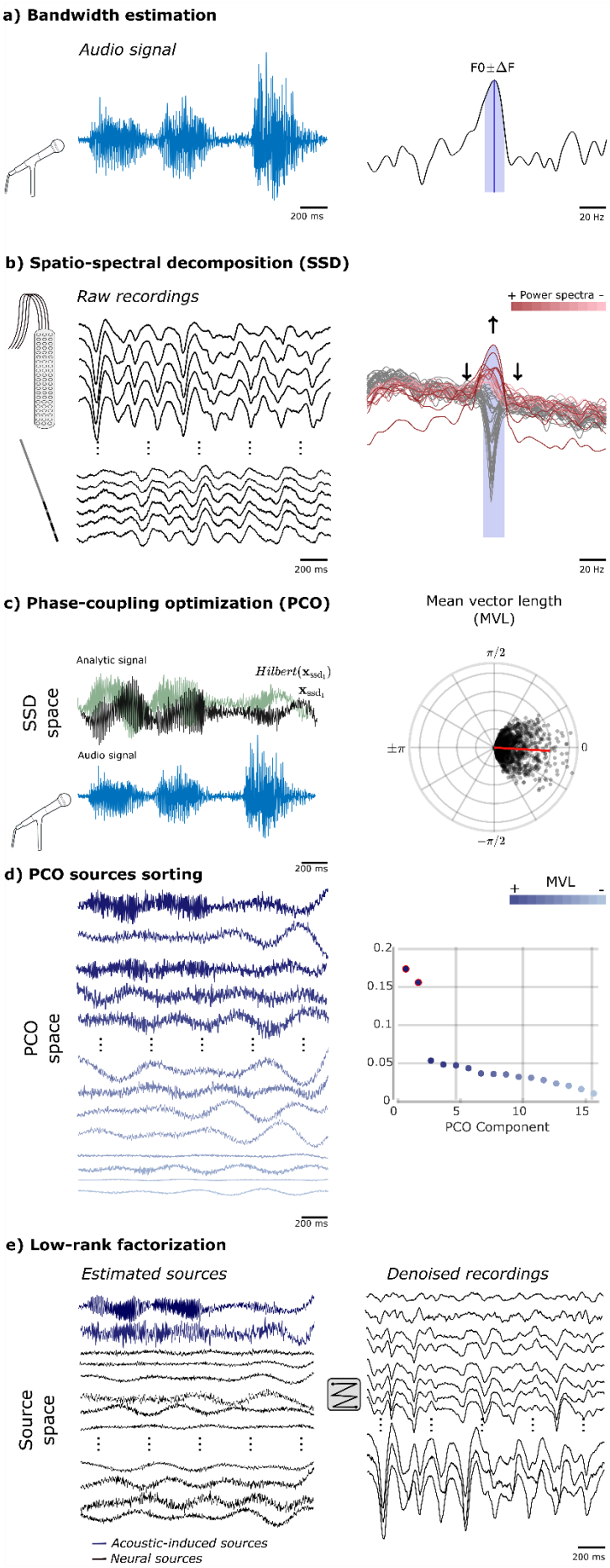

Extended Data Fig. 1 | Visualization of PCD pipeline. a) The vibration artifact bandwidth is estimated using the recorded audio, by finding the peak around F0. **b)** Once the vibration artifact bandwidth is estimated, the SSD method is applied in order to enhance the power spectral around F0. It results in as many components as the number of recorded channels, from which only a few have a power profile with maximum energy around F0. Here, the selected SSD components with a peak at F0 are color coded from dark red to pink. **c)** The phase-coupling optimization finds a linear transformation for which the coherence with the audio is maximized for each selected SSD component. **d)** PCO components are sorted according to the mean vector length, an index of coherence with the audio, and artifactual components are identified. **e)** During signal reconstruction via low-rank factorization, the artifactual components are excluded from the signal reconstruction, leading to denoised recordings.

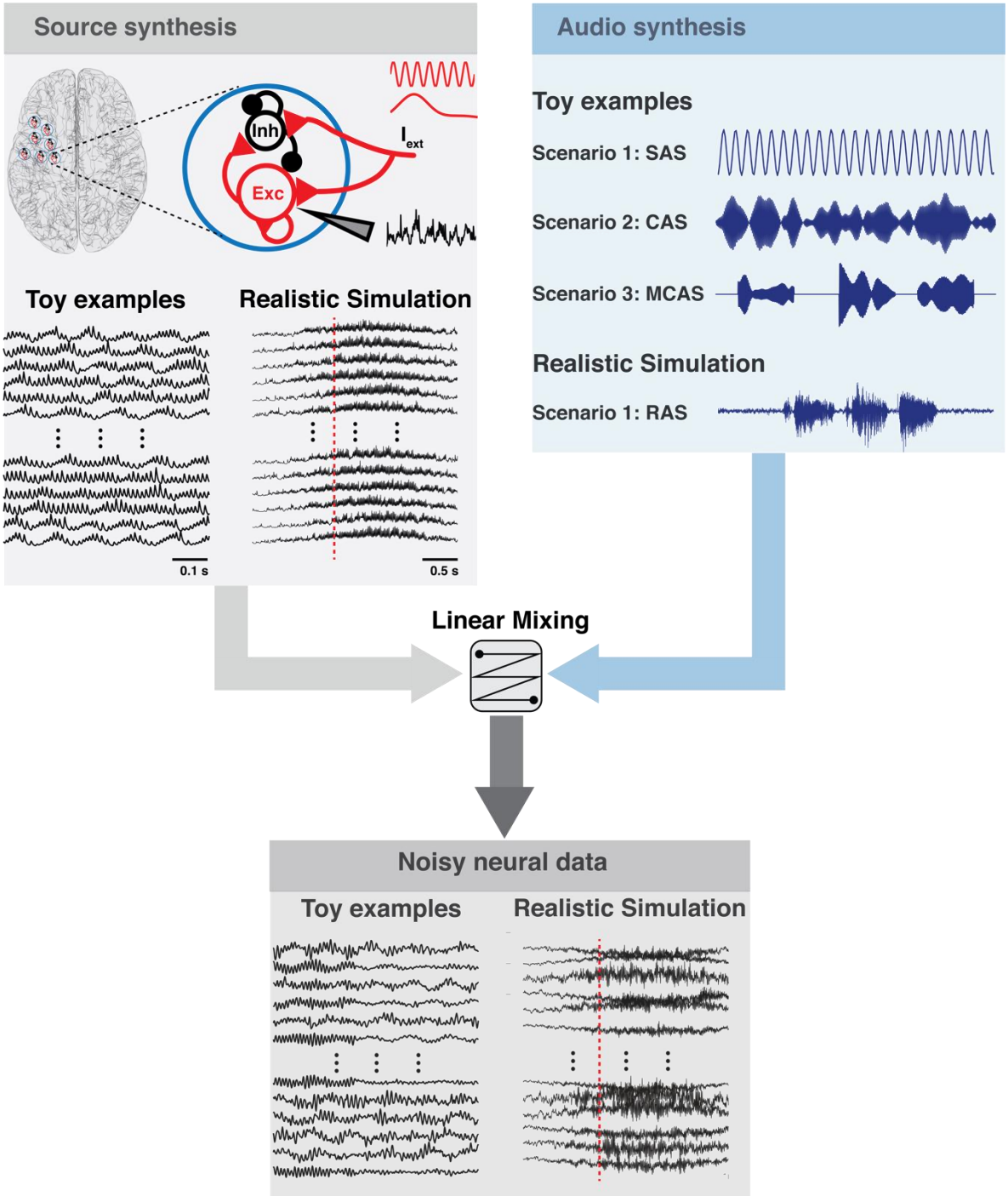

Extended Data Fig. 2 | Schematic of the pipeline for the simulation scenarios.
Brain sources are simulated using a sparse (sparseness; p = 0.2) LIF network of excitatory (N= 4000, red line) and inhibitory neurons (N = 1000, black line). Both populations receive recurrent activity and external excitatory inputs I_{ext}. I_{ext} is a Poissonian process with time-varying input rate $\nu_{ext}(t)$. The size of the synaptic connection (inhibitory: circle and excitatory: triangle) depicts the synaptic efficacy. LFPs are estimated using a simple computational proxy which neglects the direct contribution of the inhibitory population (refer to 1 for details). Simulation of neural data affected by the vibration artifact are obtained by linearly mixing brain sources and audio signal by the application of a mixing matrix. We simulated different scenarios according to the type of audio signal and the $\nu_{ext}(t)$ expression (refer to Methods for details). The vertical red dashed line depicts the onset of the speech production event.

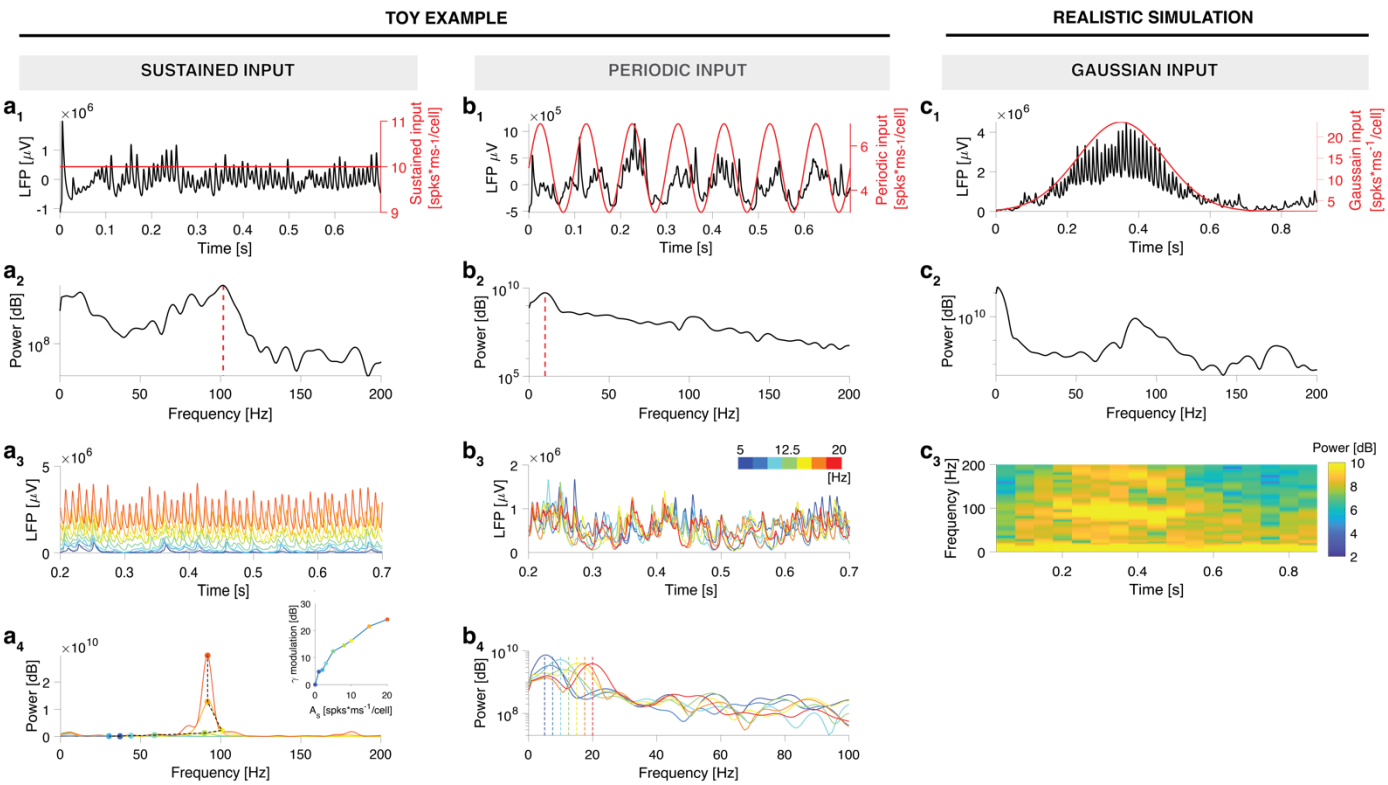

Extended Data Fig. 3 | Source activity reflects temporal properties of the network input $\nu_{signal}(t)$. $\mathbf{a_1}$- $\mathbf{a_2}$, Temporal and spectral source activity during the injection of a sustained input at 10 spikes/(ms*cell) (red line). Strong γ-oscillations are visible in the time domain with a peak at ~100 Hz (vertical red dashed line). $\mathbf{a_3}$- $\mathbf{a_4}$, gamma-oscillations entrainment can be tweaked by sweeping the intensity of the sustained input, as depicted by the color code. $\mathbf{b_1}$- $\mathbf{b_2}$, Temporal and spectral source activity during the injection of a periodically modulated input rate at 10 Hz (red line). Source activity tracks the frequency of the periodic input, revealing a peak at 10 Hz (vertical red dashed line). $\mathbf{b_3}$- $\mathbf{b_4}$, High fidelity between the frequency of the periodic input (vertical dashed line) and the peak of the oscillatory source activity, as depicted by the color code. $\mathbf{c_1}$- $\mathbf{c_3}$ Time-frequency representation of the source activity during the injection of a gaussian-modulated input. Transient gamma-oscillations emerge between 0.2 s and 0.5 s.

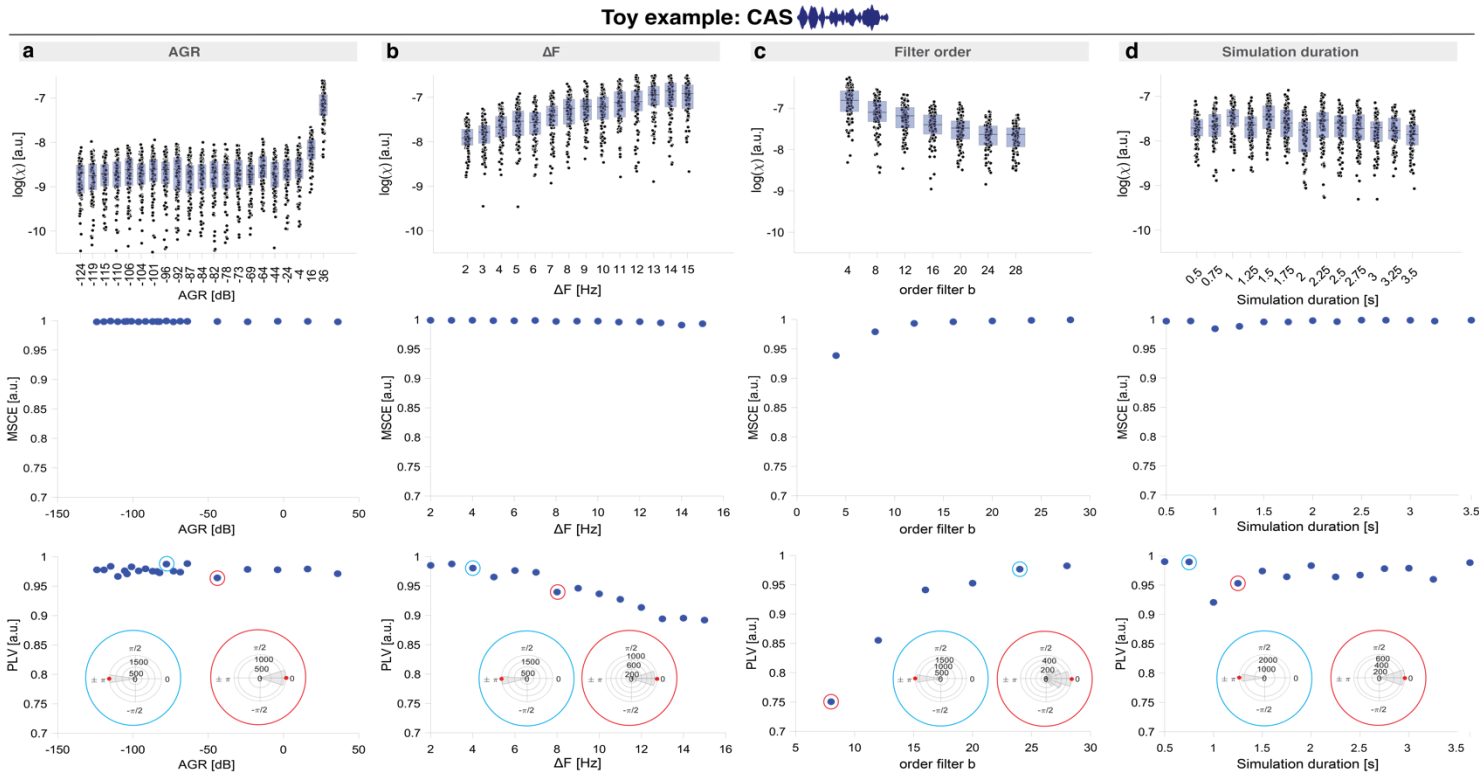

Extended Data Fig. 4 | Performances of PCD pipeline in the toy scenario CAS across a range of AGR, ΔF, filter order b and simulation duration.

a, PCD pipeline is robust to artifact-to-physiological gamma ratio (AGR) changes in terms of agreement between the ground-truth $\boldsymbol{X}_{gt}$ and cleaned data $\boldsymbol{X}$ (top, $log(\chi)$) and between the artifact $z(t)$ and the estimated artifact $z(t)_{est}$ (center-bottom, MSCE and PLV). **b-c, Broad VAFB significantly reduces PCD performances.** PCD pipeline is more accurate to remove narrowband artifacts, as suggested by the drop in performances when either the artifact frequency peak is too large (ΔF) or not well defined (order filter b) (Methods, CAS artifact definition). **d,** Duration of the simulation does not significantly impact PCD performances. Inset polar plots show the phase difference ($z(t)$ vs. $z(t)_{est}$) distribution in two exemplary simulations (red: correlation, cyan: anticorrelation), as pinpointed by surrounding circles Red filled circle displays the average.

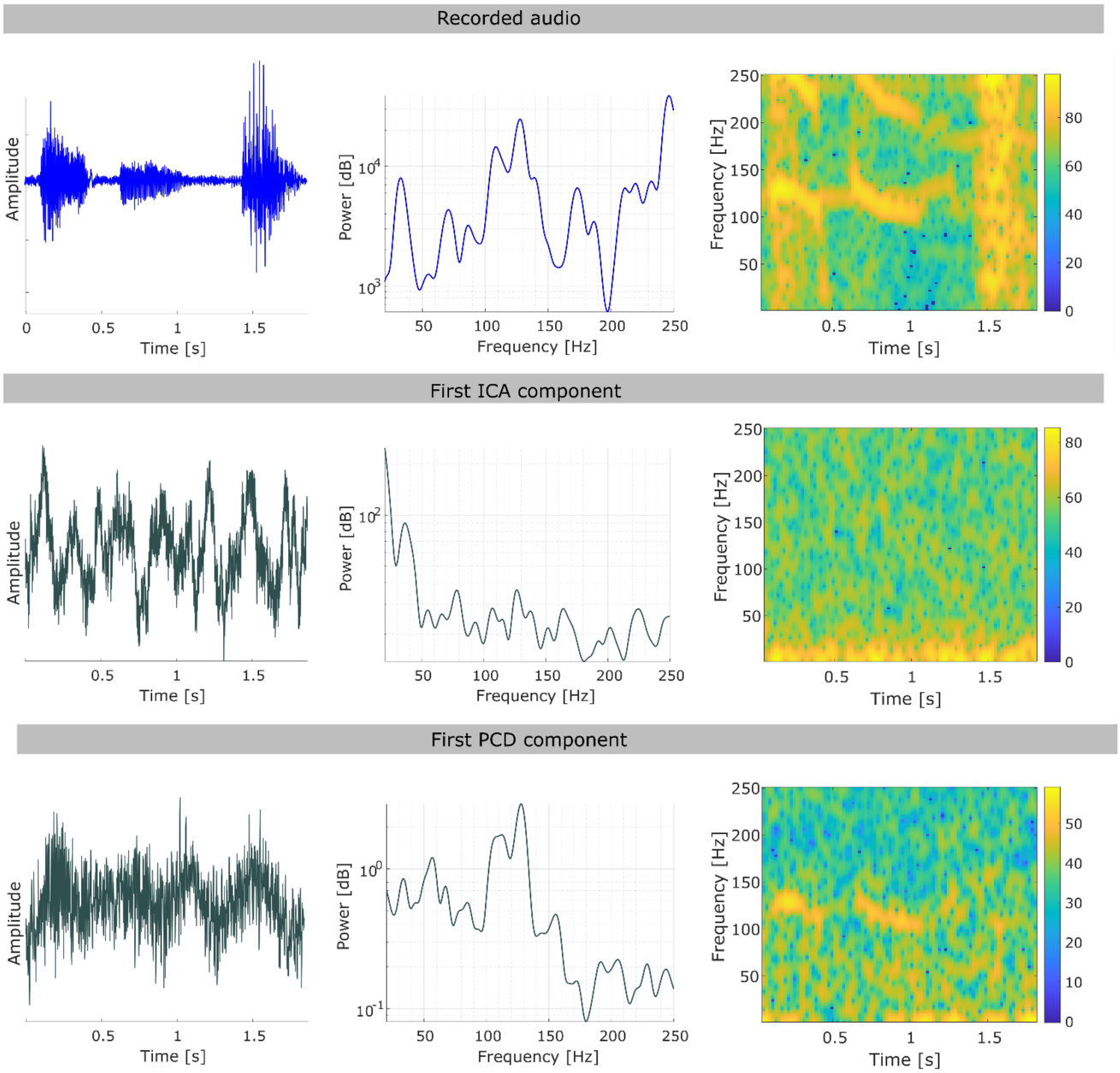

Extended Data Fig. 5 | Recorded audio and retrieved sourced by ICA and PCD.
Comparison in the temporal, frequency and time-frequency domain of the recorded audio and the first artifactual component estimated by ICA and PCD. For a given participant, at a randomly selected trial, the component with the highest phase-relationship with the audio is shown here.